Title

A genome-wide screen links peroxisome regulation with Wnt signaling through RNF146 and TNKS/2

Journal

Journal of Cell Biology, 223(10)

ISSN

0021-9525

Authors

Vu, Jonathan T

Tavasoli, Katherine U

Sheedy, Connor J

et al.

Publication Date

2024-10-07

DOI

10.1083/jcb.202312069

Title: A genome-wide screen links peroxisome regulation with Wnt signaling through RNF146 and TNKS/2

eTOC summary:
The E3 ligase RNF146 regulates peroxisomal-protein import by preventing the PARsylation of peroxisomal proteins by the poly-ADP ribose polymerases TNKS and TNKS2. Highlighting the specialization of cell-wide regulatory mechanisms at organelles, peroxisomal recruitment of TNKS/2 reorients TNKS/2 activity away from components of the Wnt/β-catenin pathway.

Authors: Jonathan T. Vu[1], Katherine U. Tavasoli[2], Connor J. Sheedy[1], Soham P. Chowdhury[2], Lori Mandjikian[2], Julien Bacal[2], Meghan A. Morrissey[2], Chris D. Richardson[2,*], Brooke M. Gardner[2,*]

Affiliations: [1]Biomolecular Science and Engineering Program, University of California, Santa Barbara, Santa Barbara, CA 93106, USA [2]Department of Molecular, Cellular, and Developmental Biology, University of California, Santa Barbara, Santa Barbara, CA 93106, USA.

* co-corresponding

Abstract:
Peroxisomes are membrane-bound organelles harboring metabolic enzymes. In humans, peroxisomes are required for normal development, yet the genes regulating peroxisome function remain unclear. We performed a genome-wide CRISPRi screen to identify novel factors involved in peroxisomal homeostasis. We found that inhibition of RNF146, an E3 ligase activated by poly(ADP-ribose), reduced the import of proteins into peroxisomes. RNF146-mediated loss of peroxisome import depended on the stabilization and activity of the poly(ADP-ribose) polymerases TNKS and TNKS2, which bind the peroxisomal membrane protein PEX14. We propose that RNF146 and TNKS/2 regulate peroxisome import efficiency by PARsylation of proteins at the peroxisome membrane. Interestingly, we found that the loss of peroxisomes increased TNKS/2 and RNF146-dependent degradation of non-peroxisomal substrates, including the beta-catenin destruction complex component AXIN1, which was sufficient to alter the amplitude of beta-catenin transcription. Together, these observations not only suggest previously undescribed roles for RNF146 in peroxisomal regulation, but also a novel role in bridging peroxisome function with Wnt/β-catenin signaling during development.

Introduction

The peroxisome is a membrane-bound organelle that harbors enzymes for specialized metabolic reactions. The most conserved peroxisomal functions include the beta-oxidation of fatty acids and regulation of reactive oxygen species [Wanders and Waterham 2006]; however, cells tune peroxisome function according to need. For example, peroxisomes in the large intestine of mice contain enzymes for optimal plasmalogen synthesis, while peroxisomes in the small intestines contain enzymes for optimal beta-oxidation of fatty acids [Morvay et al 2017]. Peroxisome function differentiates alongside cell type: for example, in inner ear cells, sound-induced autophagy of peroxisomes protects against noise overexposure [Defourny et al 2019], while in macrophages, peroxisomal metabolism improves phagocytosis [Di Cara et al 2017]. Accordingly, mutations in peroxisomal genes in humans cause a spectrum of Peroxisome Biogenesis Disorders (PBDs) with phenotypes ranging in severity from early infant mortality, developmental abnormalities, and liver dysfunction to more specific metabolic syndromes, sensorineural hearing loss, and retinal degeneration [Braverman et al 2016]. It is therefore

important to know both the genes dedicated to peroxisome function in human cells, as well as the mechanisms by which peroxisome abundance and function are coordinated to meet the needs of cell.

Peroxisomes are made and maintained by approximately 35 PEX proteins which coordinate the biogenesis of peroxisome membranes and the import of peroxisomal matrix localized enzymes. Protein import into peroxisomes depends on the presence of peroxisome structures, as well as on many of the best conserved PEX proteins that ensure the efficiency of import. Proteins tagged with a C-terminal peroxisomal targeting signal (PTS1) are recognized by the receptor PEX5, which shuttles the PTS1-cargo to the PEX13/PEX14 docking complex for import across the peroxisomal membrane [Dammai et al 2001; Skowyra et al. 2022]. After import, PEX5 is recycled via extraction by PEX1/PEX6/PEX26 from the peroxisomal membrane following ubiquitination by the PEX2/PEX10/PEX12 E3 ligase complex [Platta et al 2009; Platta et al 2005]. Cells fine tune peroxisomal protein import, and therefore peroxisome function, according to need. The repertoire of imported enzymes is regulated through transcription, as well as ribosomal readthrough that can create protein isoforms with an appended PTS1 tag [Stiebler et al 2014]. The efficiency of import is also regulated cell-wide, for example, phosphorylation of PEX5 by ATM, a DNA repair kinase, can induce peroxisome-specific autophagy in response to oxidative stress [Zhang et al 2015]. Thus, peroxisome homeostasis is tightly regulated in cells and disruption of this regulation can have severe consequences on organismal development. However, the full regulatory network that governs the steady state equilibrium of peroxisome abundance, function, and homeostasis in human cells remains elusive.

Here we performed a genome-wide CRISPRi screen in human cells to identify genes that influence the import of proteins targeted to peroxisomes. In addition to known *PEX* genes, we found that knockdown of the E3 ligase RNF146 reduces import of PTS1-tagged proteins into the peroxisome. RNF146 (Ring Finger Protein 146), also known as Iduna, is a RING-domain E3 ubiquitin ligase that recognizes and ubiquitinates proteins modified by poly(ADP-ribosyl)ation (PARsylation) [Zhang et al. 2011, DaRosa et al. 2015]. RNF146 interacts directly with poly(ADP-ribose) polymerases, such as tankyrase-1 and tankyrase-2 (TNKS and TNKS2, referred to here as TNKS/2 together) [Da Rosa et al. 2015] and PARP1 and PARP2 [Gero et al 2014, Kang et al 2011]. Together, the poly(ADP-ribose) polymerases and RNF146 specifically regulate the stability of numerous substrates which are first PARsylated and subsequently polyubiquitinated by RNF146, triggering proteasomal degradation. We found that RNF146-mediated loss of peroxisomes was dependent on the accumulation of the poly(ADP-ribose) polymerases TNKS/2, specifically by impairing import into peroxisomes through a mechanism dependent on TNKS/2's activity as poly(ADP-ribose) polymerases. We thus propose a model in which TNKS/2 binds and PARsylates PEX14 and neighboring proteins, inhibiting the import of PTS1-tagged proteins.

RNF146 and TNKS/2 are better known as co-regulators of protein stability: TNKS/2 binds and PARsylates substrates with a tankyrase-binding motif (TBM), which then triggers poly-ubiquitination by RNF146 [DaRosa et al 2015]. Known RNF146/TNKS/2 substrates include AXIN1, BLZF1, 3BP2, and CASC3 [Nie et al 2020, Levaot et al 2011]. Surprisingly, we found that in a variety of cell lines, a loss of *PEX* genes altered the stability of RNF146/TNKS/2 substrates and could therefore alter the output of downstream signaling pathways, including the Wnt/beta-catenin pathway. These observations suggest that not only is peroxisome abundance and function integrally intertwined with cell signaling pathways, but also that peroxisomes themselves regulate cellular responses to external stimuli.

Results

Sequestration of ZeoR in peroxisomes links peroxisome import to viability

Past screens for peroxisomal genes in mammalian cells have relied on peroxisome-localized enzymatic activity [Zoeller and Raetz 1986, Tsukamoto et al 1990; Morand et al. 1990] and fluorescence microscopy of PTS1-tagged fluorescent proteins [Ito et al 2000], since mammalian cells in tissue culture conditions do not require peroxisomes for growth. To facilitate a CRISPRi screening approach for regulators of peroxisome function, we engineered a cell line, which we term Pex-ZeoR, in which the efficiency of peroxisome import is linked to cell viability by fusing the fluorescent marker mVenus and a peroxisomal targeting signal (PTS1) to the gene encoding resistance to Zeocin, a 1400 Dalton molecule in the bleomycin family that induces DNA double strand breaks and causes cell death [Murray et al 2014; Drocourt et al 1990]. With this fusion construct, mVenus-ZeoR-PTS1, cells with functional peroxisomes should sequester the Zeocin resistance protein (ZeoR), thereby preventing them from neutralizing Zeocin, which is too large to passively diffuse through peroxisome membranes [Antonenkov and Hiltunen 2006]. By contrast, cells with reduced peroxisome import should accumulate mVenus-ZeoR-PTS1 in the cytoplasm where it can neutralize Zeocin, conferring a selective advantage in the presence of Zeocin (**Fig. 1A**). To affirm our strategy, we transduced HCT116 CRISPRi (dCas9-KRAB) cells [Liang et al 2018; Gilbert et al 2014] to recombinantly express mVenus-ZeoR-PTS1. As predicted, cells expressing a non-targeting control (NTC) sgRNA had fluorescent mVenus foci, while cells expressing a *PEX1* targeting sgRNA exhibited diffuse cytosolic mVenus signal (**Fig. 1B**), consistent with mVenus-ZeoR-PTS1 targeting to the peroxisome. We then assessed cell growth of the HCT116 CRISPRi Pex-ZeoR cell line over a range of Zeocin concentrations, finding a clear growth advantage for cells with sgRNAs targeting *PEX1* or *PEX6* versus NTC at high concentrations of Zeocin (**Fig. S1A**). To identify optimal selection conditions for the genome-wide screen, we performed a competition assay by co-culturing either PEX1 or PEX6 CRISPRI Pex-ZeoR cells with NTC CRISPRi Pex-ZeoR cells at varying dosages of Zeocin, and monitoring the abundance of each cell population by flow cytometry. *PEX1* and *PEX6* knockdown cells started at 5-10% of the cell population and were outcompeted by NTC cells in conditions without Zeocin. However, they displayed a marked competitive advantage in the presence of Zeocin (**Fig. 1C, Fig. S1B**). Together, these validation experiments suggest that peroxisomal sequestration of ZeoR allows for the selection of cells harboring sgRNAs that target peroxisomal genes.

A genome-wide CRISPRi screen in Pex-ZeoR cells enriches known *PEX* genes

Emboldened, we executed a genome-wide screen with the Pex-ZeoR cell line to identify novel genes that affect peroxisomal homeostasis. Infection with a genome-wide CRISPRi library was followed by chronic treatment with or without Zeocin, combined with regular passaging of cells over 35 days, with samples collected every 7 days for terminal Illumina sequencing preparation (**Fig. S1C**). We found 1,717 genes that were significantly different (p<0.05) between the treated and untreated conditions at the day 14 timepoint (**Fig. 1D**). Day 14 serves as the optimal comparison timepoint because of clear enrichment of the majority of known *PEX* genes while maintaining sufficient library diversity and replicate quality (**Fig. S1D, S1E**).

We observed enrichment of guides targeting known *PEX* genes that facilitate PTS1 import (*PEX5, PEX13, PEX14, PEX2/PEX12, PEX1/PEX6, PEX26*) and peroxisome membrane protein targeting (*PEX19*) affirming the efficacy of our strategy (**Fig. 1D**). Guides targeting *PEX7* and alpha and beta variants of *PEX11* were not strongly enriched, consistent with roles in recognition of the alternative PTS2 targeting signal (*PEX7*) [Braverman et al 1997], and peroxisomal membrane elongation (*PEX11*) [Koch et al 2010]. Guides targeting one component of the peroxisome RING finger complex, PEX10, were not enriched compared to the other constituents, PEX2 and PEX12, and guides targeting other peroxisome membrane biogenesis factors PEX3 and PEX16, were depleted in the screen (**Fig. 1D, S1E**). While initially

unexpected, these results align with recent data that PEX10 and PEX16 CRISPR/Cas knockouts display only partial peroxisomal import defects (Yagita et al 2022; Ott et al 2023). Of the known factors regulating peroxisome specific autophagy, such as NBR1, MARCH5, SQSTM1, HIF1A, and NIX [Kim et al 2008, Deosaran et al 2013, Zheng et al 2022, Wilhelm et al 2022], we found that only guides targeting *HIF1A*, the loss of which stabilizes peroxisomes [Wilhelm et al 2022], were strongly depleted in our screen. Although most peroxisome-homeostasis related genes behaved according to our predictions, a handful did not align with our a priori prognosis. Our results suggest the possibility that not all of the aforementioned genes are simple or monotonic in their effect on peroxisome import or autophagy, representing potential new mechanisms for further investigation.

Guides targeting *RNF146, INTS8, KCNN4* reduce peroxisomal foci intensity

We anticipated that sgRNAs that improve resistance to Zeocin independent of the peroxisomal localization of ZeoR should also be significantly enriched in our dataset. Thus, to narrow the candidate list to genes relevant to peroxisomal localization of ZeoR, we filtered our screen results to exclude factors that modulated resistance to a related DNA damaging agent, bleomycin [Olivieri et al 2020] (**Fig. S1F, Table S1**, Z-score range [-0.5,0.5]). GO analysis of the remaining genes with a fold change greater than 2 and a Mann-Whitney $p<0.05$ revealed a 100-fold enrichment of GO terms related to protein import into the peroxisome, and a greater than 20-fold enrichment related to RNA cleavage involved in mRNA processing (**Table S2**). We note that several *PEX* genes (*PEX1, PEX6, PEX12*) modulate bleomycin resistance, possibly because there is a direct link between DNA repair and peroxisome biology through localization of the DNA repair kinase ATM to peroxisome membranes [Zhang et al 2015].

We then used fluorescence microscopy of mVenus-PTS1 in the Pex-ZeoR cell line to assess how knockdown of candidate genes altered peroxisome abundance. For each candidate gene, we produced two unique constitutive knockdown cell lines per gene and quantified mVenus-PTS1 foci number, foci and cell area, and foci and cytoplasm fluorescence intensity using CellProfiler [Stirling et al. 2021]. To estimate the efficiency of peroxisome import while accounting for different mVenus-PTS1 expression levels, we calculated the ratio of the intensity of mVenus-PTS1 in peroxisome foci to the intensity of mVenus-PTS1 in the cytoplasm (**Fig. 2A, S2A, S2B**). We found that several of the guides enriched by Zeocin selection decreased the ratio of peroxisomal to cytosolic mVenus-PTS1 intensity, including those targeting the E3 ligase RNF146, Integrator complex subunit INTS8, and calcium-activated potassium channel KCNN4 (**Fig. 2A**).

RNF146 regulates peroxisome foci intensity in multiple cell lines

Given the magnitude of the impact of the RNF146 knockdown on mVenus-PTS1 foci (**Fig. 2A, 2B**), we chose to focus our efforts on characterizing the effects of RNF146 on peroxisome homeostasis. We first ruled out possible off-target effects of the RNF146 sgRNA by treating our reporter cell line with RNF146 siRNA, which recapitulated the loss of mVenus foci signal within 24 hours of siRNA treatment (**Fig. 2C**). To determine if the peroxisomal effect of RNF146 knockdown was specific to the HCT116 cell line, we created a secondary cell line, the H4 astrocytoma cancer cell line, harboring the same CRISPRi machinery and our Pex-ZeoR reporter. We observed significant depletion of mVenus-PTS1 foci intensity in both the HCT116 and H4 *RNF146* and *PEX* knockdown cell lines (**Fig. 2B, 2D**). The significant depletion of PTS1 foci in two independent cell lines suggests that RNF146 has a bona fide role in regulating peroxisome homeostasis in human cells.

To determine if *RNF146* KD impacted peroxisome biogenesis through an effect on *PEX* gene expression, we gathered RNA-seq data of *RNF146* KD HCT116 cell mRNA transcripts

versus NTC cells. We found that knockdown of *RNF146*, which was confirmed in the data set, mildly repressed transcription of *PEX3* and *PEX10*. Given that neither *PEX3* nor *PEX10* had positive phenotype scores in the CRISPRi screen, we found it unlikely that the RNF146 phenotype can be completely explained by these transcriptional changes, thereby indicating a post-transcriptional role for RNF146 in regard to peroxisomal homeostasis (**Fig. 2E**).

RNF146-mediated loss of mVenus-PTS1 foci depends on TNKS/2, but not autophagy

RNF146 is known to collaborate with poly(ADP-ribose) polymerases to ubiquitinate PARsylated proteins and target them for degradation. Loss of RNF146 is therefore expected to stabilize PARsylated substrates, which could act to either inhibit peroxisome biogenesis or increase peroxisome-specific autophagy. We therefore tested if the observed loss of mVenus-PTS1 foci in response to RNF146 knockdown depended on changes in the RNF146 partners TNKS/2. We first assessed TNKS/2 levels in an RNF146 knockdown, and found that knockdown of RNF146 expression in the HCT116 Pex-ZeoR cell line caused a marked increase in TNKS/2 protein levels (**Fig. 3A**). To test if RNF146's effect on peroxisomes depended on increased TNKS/2 levels, we performed a dual knockdown assay of *RNF146* and *TNKS/2* in our reporter cell line. We found that siRNA knockdown of *TNKS and TNKS2* in RNF146 CRISPRi cells rescued the import of mVenus-PTS1 (**Fig. 3A, 3B**) indicating that RNF146's effect on peroxisomes depended on TNKS/2. In an extended assay, we attempted to swap the dual KD strategies of RNF146 and TNKS, such that only TNKS (and not TNKS2) was suppressed by CRISPRi, and RNF146 expression was suppressed by siRNA treatment. We observed that there was clear rescue in the TNKS CRISPRi and RNF146 siRNA treatment, but that this rescue was not as complete as the RNF146 CRISPRi and TNKS/2 siRNA treatment, suggesting that TNKS2 may also play a role in the RNF146 KD phenotype (**Fig. S3A**). These results are consistent with previous reports that TNKS is significantly stabilized in cells lacking RNF146 [Nie et al 2020]. Although it was previously shown that TNKS mediates peroxisome-specific autophagy [Li et al 2017], we found that siRNA inhibition of ATG7 did not prevent the accumulation of TNKS/2 nor the loss of mVenus-PTS1 foci intensity in RNF146 knockdown cells **(Fig. 3C, 3D**). This lack of dependence on autophagy was further corroborated in multiple cell lines by the treatment of RNF146 knockdown cells with autophagy inhibitors bafilomycin or hydroxychloroquine, which, despite preventing LC3BII turnover, did not substantially rescue peroxisome foci number or intensity relative to control cells **(Fig. S3B-G)**. These observations suggest that while the effect of RNF146 knockdown on peroxisomes depends on TNKS/2, it does not depend on peroxisome-specific autophagy.

Loss of RNF146 specifically inhibits import into peroxisomes

Since the loss of RNF146 did not appear to induce peroxisome-specific autophagy, we evaluated whether the loss of RNF146 could specifically impair peroxisome biogenesis at the stage of protein import into peroxisomes. We performed immunofluorescence microscopy on the HCT116 and H4 CRISPRi Pex-ZeoR cell lines harboring sgRNAs for *NTC, RNF146, PEX5*, and *PEX19*, where PEX5 and PEX19 are the receptors for PTS1-tagged matrix protein import and peroxisomal membrane protein insertion, respectively **(Fig. 4A, S4A**). We found that knockdown of RNF146 in both HCT116 and H4 cells resembled a PEX5 knockdown, in which a peroxisome membrane protein PMP70 remains present and punctate **(Fig. 4A, 4B, S4A, S4B**), but matrix proteins, both mVenus-PTS1 and catalase, no longer form foci **(Fig. 4A, 4C, Fig. S4A, S4C**) or co-localize with PMP70 **(Fig. S4D**). These observations suggest that loss of RNF146 inhibits import of PEX5 client proteins into the peroxisome.

Efficient peroxisomal matrix protein import relies on PEX5 binding to the PTS1-tagged protein, PEX5 docking to PEX13/PEX14 at the peroxisome, and extraction of ubiquitinated

PEX5 from the peroxisome membrane by the PEX1/PEX6/PEX26 motor complex for continued rounds of import. PEX5 is therefore typically distributed between both cytoplasmic and membrane fractions, with an increased proportion at the peroxisome membrane in mutants of the ubiquitination and extraction machinery [Platta et al 2005]. To determine if RNF146 knockdown alters the localization of PEX5, we probed for PEX5, mVenus-SKL, and catalase in soluble and membrane fractions after fractionation. As expected, we observed that PEX5 distributes between both membrane and soluble fractions in wild type cells. Interestingly, a larger proportion of PEX5 was soluble in RNF146 knockdown cells compared to controls cells **(Fig. 4D)**. This suggests that the impairment of import of peroxisomes may be due to reduced recruitment of PEX5 and PTS1-cargo to the peroxisome membrane. Additionally, we observed that the soluble proportion of mVenus-SKL and catalase, both PEX5 client proteins with and without, respectively, a canonical PTS1 tag, increased in RNF146 and PEX5 knockdown cells, confirming that RNF146 knockdown also impedes import of endogenous matrix proteins **(Fig. 4D).**

PARP activity of TNKS/2 impedes import into peroxisomes

TNKS/2 contains N-terminal ankyrin repeats that bind substrates with a TBM, a SAM domain that mediates oligomerization, and a C-terminal poly(ADP-ribose) polymerase domain [Guettler et al 2011]. There are predicted, conserved TBMs in PEX14, PEX5, PEX19, and PEX11G [Guettler et al 2011]. Specifically, PEX14 was predicted to have at least 4 purported TBMs (**Fig. S4E**). We found that TNKS/2 co-immunoprecipitated both FLAG-PEX14 and PEX5 upon RNF146 knockdown **(Fig. 5A)**. Additionally, when the reciprocal experiment was performed, full length FLAG-PEX14 co-immunoprecipitated TNKS/2 and PEX5 in NTC and RNF146 knockdown cells. Notably, when the TBM3 of PEX14 was mutated, FLAG-PEX14-ΔTBM3 cells had reduced affinity for TNKS/2 interaction **(Fig. S4E)**. These results suggest TNKS/2 associates with the peroxisome membrane and peroxisome import machinery, such as PEX14, upon RNF146 knockdown.

To test if RNF146's effect on peroxisome import depended on the PARP activity of TNKS/2, we tested if the TNKS/2 inhibitors G007LK and XAV939 restored peroxisome foci in RNF146 knockdown cells **(Fig. 5B, 5C)**. We found that TNKS/2 inhibitors partially restored import of mVenus-PTS1 into foci in RNF146 knockdown cells as judged by the ratio of foci to cytosolic intensity of mVenus-PTS1, but did not fully recover peroxisome number **(Fig. 5C)**. To determine if TNKS/2 PARsylated proteins at the peroxisome membrane, we immunoprecipitated PEX14-FLAG. We found that proteins in the PEX14-FLAG elution, which included PEX14-FLAG, PEX13, PEX5, and TNKS, were PARsylated (**Fig. 5D)**. While it is unclear exactly which proteins are PARsylated, PARsylation was sensitive to TNKS/2 inhibitor XAV939 and amplified by RNF146 knockdown (**Fig. 5D)**. In addition, we found that suppression of RNF146 and the concomitant increase of TNKS/2 resulted in lowered steady state levels of PEX14 and PEX13, but not peroxisome membrane protein PMP70, and that this effect was abrogated when TNKS/2 was inhibited by XAV939 (**Fig. 5E**). All together, these observations suggest that TNKS/2's PARsylation activity is important for RNF146's effect on peroxisomes. We therefore propose a model in which high levels of active TNKS/2, induced by loss of RNF146, binds PEX14 and PARsylates proteins at the peroxisome membrane, which inhibits PEX5-mediated protein import into peroxisomes (**Fig. 5F)**.

PEX proteins alter RNF146/TNKS/2 activity towards other substrates

This model suggests that TNKS/2 binds peroxisome membrane protein PEX14 and can localize to the peroxisome. Other better-known substrates of TNKS/2, such as BLZF1, which localizes to the Golgi [Yue et al 2021], and AXIN1, which localizes to centrosomes [Lach et al

2022], have defined locations elsewhere in the cell. We thus wondered if peroxisomal recruitment of TNKS/2 could regulate access to other substrates. To test if the presence of peroxisome membranes and membrane proteins alters TNKS/2 substrate selection, we evaluated the stability of the TNKS/2/RNF146 substrates AXIN1, CASC3, and BLZF1 in cells with knockdown of the peroxisomal membrane protein *PEX14*, the peroxisomal membrane protein chaperone *PEX19*, or a non-targeting control (NTC). We found that AXIN1 and CASC3 levels were significantly depleted in *PEX19* knockdown HCT116 cells, and BLZF1 levels were depleted in both *PEX19* and *PEX14* knockdown HCT116 cells (**Fig. 6A**). Furthermore, *PEX14* and *PEX19* knockdowns also depleted AXIN1 levels in HEK293T, iPSC AICS-0090-391, and H4 CRISPRi cells (**Fig. 6B, 6C, Fig. S5A**), illustrating that this phenomenon is not specific to HCT116 cells. To confirm that the effect of *PEX19* knockdown arises from loss of PEX19, we re-expressed PEX19 using a lentiviral vector to complement the knockdown of endogenous *PEX19*, and observed a rescue of AXIN1 stability (**Fig. 6D**). Additionally, suppression of either *RNF146* or *TNKS/2* mRNA transcripts via siRNA, as well as XAV939-mediated catalytic inhibition of TNKS/2, restored AXIN1 stability in *PEX19* knockdown cells, demonstrating that loss of PEX19 activates RNF146/TNKS/2-mediated destabilization of AXIN1 (**Fig. 6D**). These observations suggest that functional peroxisomes repress TNKS/2 activity towards some substrates, including AXIN1, BLZF1, and CASC3.

Increased Wnt/beta-catenin signaling in *PEX* knockdown cells

AXIN1 is the limiting component for the formation of the beta-catenin destruction complex which induces the phosphorylation and subsequent degradation of the beta-catenin transcription factor. In canonical Wnt signaling, Wnt ligand binding to the Frizzled receptor dissociates the beta-catenin destruction complex, allowing beta-catenin to accumulate, enter the nucleus, and induce transcription of Wnt-responsive genes. The stabilization of AXIN1, such as by TNKS/2 inhibitors, inhibits Wnt signaling by increasing levels of the destruction complex [Huang et al 2009]. Since AXIN1 was severely destabilized in *PEX19* knockdown HCT116 cells and partially destabilized in *PEX14* and *PEX19* knockdown HEK293T, H4, and iPSC AICS-0090-391 cells, we tested if the knockdown of *PEX* genes can therefore influence the Wnt signaling pathway using the TOPFlash reporter for beta-catenin transcriptional activity. We found that HCT116 cells had a greater transcriptional response to Wnt ligand in *PEX14* and *PEX19* knockdown cells (**Fig. 6E**), as well as increased basal activity. Since HCT116 cells are derived from a colorectal carcinoma heterozygous for a dominant mutation in beta-catenin that causes constitutively active beta-catenin-TCF regulated transcription [Morin et al 1997], we also tested the effect of the PEX knockdowns on the TOPFlash reporter in HEK293T cells. Both *PEX14* and *PEX19* knockdown HEK293Ts exhibited a partial loss of AXIN1 levels (**Fig. 6B**), and consistently, also exhibited a greater response to Wnt ligand, though basal levels were not perturbed (**Fig. 6F**). Our observations show that knockdown of *PEX14* and *PEX19* increases Wnt signaling consistent with the decreased levels of the core subunit of the beta-catenin destruction complex, AXIN1.

Discussion

Here we describe an approach to link cell viability to peroxisome import efficiency by sequestering the Zeocin resistance protein in the peroxisome. We use this approach to screen for novel genes regulating peroxisome import efficiency. In addition to known PEX genes, we found that the E3 ligase RNF146 regulates peroxisome import through its control of the levels of the poly(ADP-ribose) polymerases TNKS/2. High levels of TNKS/2, which can bind PEX14 and possibly other PEX proteins, specifically inhibits import into peroxisomes. In our cell lines, inhibition of import depends on TNKS/2's poly(ADP-ribose) polymerase activity. We note that Li and colleagues showed that increased levels of TNKS/2 due to treatment with TNKS/2 inhibitors

such as XAV939 could induce peroxisome-specific autophagy in HEK-293T cells; however, this autophagy does not mediate the loss of mVenus-PTS1 foci in response to RNF146 knockdown in H4 or HCT116 cells. Instead, we find that TNKS/2's polymerase activity is required for the observed inhibition of peroxisome import. We therefore propose a model in which loss of RNF146 stabilizes active TNKS/2, which PARsylates proteins at the peroxisome membrane and impairs their function in matrix protein import into the peroxisome.

This model suggests that any mechanism that inactivates RNF146 will inhibit import into peroxisomes. In mice, RNF146 transcription is repressed during RANKL-mediated osteoclastogenesis through an NF-κB binding site [Matsumoto et al 2017], suggesting that peroxisome import may be coordinated with cell type specification through RNF146 and TNKS/2. RNF146 activity is also regulated by sumoylation [Li et al 2023], localization to the nucleus [Gero et al 2014; Sheng et al 2018], and direct interaction with other poly(ADP-ribose) polymerases such as PARP-1 [Gero et al 2014]. It is therefore possible that temporary localization of RNF146 to the nucleus in response to DNA damage could impede peroxisome import, perhaps to increase concentrations of cytosolic catalase to reduce oxidative stress. The effect of this regulation on TNKS/2 activity and peroxisome import, and the consequences for RNF146's protective role during DNA damage [Kang et al 2011], oxidative stress [Xu et al 2013], and PARsylation induced cell death [Andrabi et al 2011] warrants further investigation.

A second implication of our results is that RNF146/TNKS/2 together may regulate the stability of substrates at the peroxisome membrane, such as PEX14 itself, or neighboring proteins. Proteomic studies show that the loss of TNKS significantly stabilizes PEX14 and SLC27A2, a peroxisomal transporter for long chain fatty acids [Bhardwaj et al 2017], and indeed, we observed that high levels of TNKS induced by RNF146 knockdown destabilized PEX14 and PEX13 (Fig. 5D). We did not observe a change in peroxisome protein import or peroxisome number in response to TNKS knockdown (**Fig. 3B**). However, it is possible that this may be due to the relatively low levels of expression of endogenous TNKS in the HCT116 cell line, and in cells with high levels of TNKS, such as the brain, adipose tissue, and endocrine pancreas [Yeh et al 2009], it is possible that a knockdown of TNKS could improve peroxisome import and abundance. Indeed, studies of TNKS-deficient mice show that they have increased fatty acid oxidation, which is consistent with improved peroxisomal function [Yeh et al 2009]. It is also possible that RNF146/TNKS activity at the peroxisome membrane regulates signaling from the peroxisome membrane. For example, RNF146/TNKS coordinate the degradation of the antiviral protein MAVS [Xu et al 2022], which has been shown to localize to both the peroxisome and mitochondria and initiate disparate signaling pathways upon viral infection [Dixit et al 2010].

An intriguing corollary of RNF146/TNKS localization to the peroxisome membrane is the impact of this localization on its access to other substrates. We found that the knockdown of different PEX proteins, particularly PEX14, which binds TNKS, and PEX19, which is generally required for peroxisome membrane protein stability, decreases the stability of RNF146/TNKS substrates that are not thought to be at the peroxisome. We propose that localization to the peroxisome membrane acts as a sink for RNF146/TNKS, keeping RNF146/TNKS away from other substrates such as AXIN1 and Golgi-localized BLZF1, and thereby stabilizing them. In this model, the absence of peroxisomes allows RNF146/TNKS to re-localize to induce the degradation of AXIN1 and BLZF1. Indeed, reports in the literature suggest that both RNF146 and TNKS can re-localize in response to perturbations; RNF146 moves between the cytoplasm and nucleus in response to oxidative stress and DNA damage [Gero et al 2014; Kang et al 2011] and TNKS's diffuse cytosolic localization becomes punctate with treatment with TNKS inhibitors [Martino-Echarri et al 2016, Thorvaldsen et al 2015] and infection with Sendai virus [Xu et al 2022].

Finally, we demonstrated that the effect of PEX knockdowns on the RNF146/TNKS substrate AXIN1 was sufficient to alter the transcriptional response to Wnt ligand in two different cell lines. Our results suggest that peroxisomes may act as signaling platforms that can alter cell

fate decisions by impacting Wnt signaling. The most severe forms of Zellweger syndrome have stereotyped neuronal migration disorders, chondrodysplasia punctata, renal cysts, and craniofacial dysmorphisms indicating disruptions to normal development [Braverman et al 2016]. Our findings raise the possibility that the perturbation of developmental signaling pathways contributes to the pathology of Zellweger Spectrum Disorders.

References

Andrabi, S.A., H.C. Kang, J.-F. Haince, Y.-I. Lee, J. Zhang, Z. Chi, A.B. West, R.C. Koehler, G.G. Poirier, T.M. Dawson, and V.L. Dawson. 2011. Iduna protects the brain from glutamate excitotoxicity and stroke by interfering with poly(ADP-ribose) polymer-induced cell death. *Nat Med*. 17:692–699. doi:10.1038/nm.2387.

Antonenkov, V.D., and J.K. Hiltunen. 2006. Peroxisomal membrane permeability and solute transfer. *Biochimica et Biophysica Acta (BBA) - Molecular Cell Research*. 1763:1697–1706. doi:10.1016/j.bbamcr.2006.08.044.

Bhardwaj, A., Y. Yang, B. Ueberheide, and S. Smith. 2017. Whole proteome analysis of human tankyrase knockout cells reveals targets of tankyrase-mediated degradation. *Nat Commun*. 8:2214. doi:10.1038/s41467-017-02363-w.

Braverman, N., G. Steel, C. Obie, A. Moser, H. Moser, S.J. Gould, and D. Valle. 1997. Human PEX7 encodes the peroxisomal PTS2 receptor and is responsible for rhizomelic chondrodysplasia punctata. *Nat Genet*. 15:369–376. doi:10.1038/ng0497-369.

Braverman, N.E., G.V. Raymond, W.B. Rizzo, A.B. Moser, M.E. Wilkinson, E.M. Stone, S.J. Steinberg, M.F. Wangler, E.T. Rush, J.G. Hacia, and M. Bose. 2016. Peroxisome biogenesis disorders in the Zellweger spectrum: An overview of current diagnosis, clinical manifestations, and treatment guidelines. *Molecular Genetics and Metabolism*. 117:313–321. doi:10.1016/j.ymgme.2015.12.009.

Chen, X., and R. Prywes. 1999. Serum-Induced Expression of the *cdc25A* Gene by Relief of E2F-Mediated Repression. *Molecular and Cellular Biology*. 19:4695–4702. doi:10.1128/MCB.19.7.4695.

Chen, S., Zhou, Y., Chen, Y., Gu, J., fastp: an ultra-fast all-in-one FASTQ preprocessor, *Bioinformatics*, Volume 34, Issue 17, September 2018, Pages i884–i890, https://doi.org/10.1093/bioinformatics/bty560

Dammai, V., and S. Subramani. 2001. The Human Peroxisomal Targeting Signal Receptor, Pex5p, Is Translocated into the Peroxisomal Matrix and Recycled to the Cytosol. *Cell*. 105:187–196. doi:10.1016/S0092-8674(01)00310-5.

DaRosa, P.A., Z. Wang, X. Jiang, J.N. Pruneda, F. Cong, R.E. Klevit, and W. Xu. 2015. Allosteric activation of the RNF146 ubiquitin ligase by a poly(ADP-ribosyl)ation signal. *Nature*. 517:223–226. doi:10.1038/nature13826.

Defourny, J., A. Aghaie, I. Perfettini, P. Avan, S. Delmaghani, and C. Petit. 2019. Pejvakin-mediated pexophagy protects auditory hair cells against noise-induced damage. *Proc. Natl. Acad. Sci. U.S.A.* 116:8010–8017. doi:10.1073/pnas.1821844116.

Deosaran, E., K.B. Larsen, R. Hua, G. Sargent, Y. Wang, S. Kim, T. Lamark, M. Jauregui, K. Law, J. Lippincott-Schwartz, A. Brech, T. Johansen, and P.K. Kim. 2012. NBR1 acts as an autophagy receptor for peroxisomes. *Journal of Cell Science*. jcs.114819. doi:10.1242/jcs.114819.

Di Cara, F., A. Sheshachalam, N.E. Braverman, R.A. Rachubinski, and A.J. Simmonds. 2017. Peroxisome-Mediated Metabolism Is Required for Immune Response to Microbial Infection. *Immunity*. 47:93-106.e7. doi:10.1016/j.immuni.2017.06.016.

Dixit, E., S. Boulant, Y. Zhang, A.S.Y. Lee, C. Odendall, B. Shum, N. Hacohen, Z.J. Chen, S.P. Whelan, M. Fransen, M.L. Nibert, G. Superti-Furga, and J.C. Kagan. 2010. Peroxisomes Are Signaling Platforms for Antiviral Innate Immunity. *Cell*. 141:668–681. doi:10.1016/j.cell.2010.04.018.

Dobin A, Davis CA, Schlesinger F, Drenkow J, Zaleski C, Jha S, Batut P, Chaisson M, Gingeras TR. STAR: ultrafast universal RNA-seq aligner. Bioinformatics. 2013 Jan 1;29(1):15-21. doi: 10.1093/bioinformatics/bts635. Epub 2012 Oct 25. PMID: 23104886; PMCID: PMC3530905.

Drocourt, D., T. Calmels, J.-P. Reynes, M. Baron, and G. Tiraby. 1990. Cassettes of the *Streptoalloteichus hindustanus ble* gene for transformation of lower and higher eukaryotes to phleomycin resistance. *Nucl Acids Res*. 18:4009–4009. doi:10.1093/nar/18.13.4009.

Gerö, D., P. Szoleczky, A. Chatzianastasiou, A. Papapetropoulos, and C. Szabo. 2014. Modulation of Poly(ADP-Ribose) Polymerase-1 (PARP-1)-Mediated Oxidative Cell Injury by Ring Finger Protein 146 (RNF146) in Cardiac Myocytes. *Mol Med*. 20:313–328. doi:10.2119/molmed.2014.00102.

Gilbert, L.A., M.A. Horlbeck, B. Adamson, J.E. Villalta, Y. Chen, E.H. Whitehead, C. Guimaraes, B. Panning, H.L. Ploegh, M.C. Bassik, L.S. Qi, M. Kampmann, and J.S. Weissman. 2014. Genome-Scale CRISPR-Mediated Control of Gene Repression and Activation. *Cell*. 159:647–661. doi:10.1016/j.cell.2014.09.029.

Guettler, S., J. LaRose, E. Petsalaki, G. Gish, A. Scotter, T. Pawson, R. Rottapel, and F. Sicheri. 2011. Structural Basis and Sequence Rules for Substrate Recognition by Tankyrase Explain the Basis for Cherubism Disease. *Cell*. 147:1340–1354. doi:10.1016/j.cell.2011.10.046.

Horlbeck, M.A., L.A. Gilbert, J.E. Villalta, B. Adamson, R.A. Pak, Y. Chen, A.P. Fields, C.Y. Park, J.E. Corn, M. Kampmann, and J.S. Weissman. 2016. Compact and highly active next-generation libraries for CRISPR-mediated gene repression and activation. *eLife*. 5:e19760. doi:10.7554/eLife.19760.

Huang, S.-M.A., Y.M. Mishina, S. Liu, A. Cheung, F. Stegmeier, G.A. Michaud, O. Charlat, E. Wiellette, Y. Zhang, S. Wiessner, M. Hild, X. Shi, C.J. Wilson, C. Mickanin, V. Myer, A. Fazal, R. Tomlinson, F. Serluca, W. Shao, H. Cheng, M. Shultz, C. Rau, M. Schirle, J. Schlegl, S. Ghidelli, S. Fawell, C. Lu, D. Curtis, M.W. Kirschner, C. Lengauer, P.M. Finan, J.A. Tallarico, T. Bouwmeester, J.A. Porter, A. Bauer, and F. Cong. 2009. Tankyrase inhibition stabilizes axin and antagonizes Wnt signalling. *Nature*. 461:614–620. doi:10.1038/nature08356.

Ito, M., R. Ito, Y. Huang, S. Miura, A. Imamura, Y. Suzuki, and N. Shimozawa. 2000. Rapid isolation and characterization of CHO mutants deficient in peroxisome biogenesis using the peroxisomal forms of fluorescent proteins. *Biochimica et Biophysica Acta (BBA) - Molecular Cell Research*. 1496:232–242. doi:10.1016/S0167-4889(00)00019-7.

Kampmann, M., M.C. Bassik, and J.S. Weissman. 2014. Functional genomics platform for pooled screening and generation of mammalian genetic interaction maps. *Nat Protoc*. 9:1825–1847. doi:10.1038/nprot.2014.103.

Kang, H.C., Y.-I. Lee, J.-H. Shin, S.A. Andrabi, Z. Chi, J.-P. Gagné, Y. Lee, H.S. Ko, B.D. Lee, G.G. Poirier, V.L. Dawson, and T.M. Dawson. 2011. Iduna is a poly(ADP-ribose) (PAR)-dependent E3 ubiquitin ligase that regulates DNA damage. *Proc. Natl. Acad. Sci. U.S.A.* 108:14103–14108. doi:10.1073/pnas.1108799108.

Kim, P.K., D.W. Hailey, R.T. Mullen, and J. Lippincott-Schwartz. 2008. Ubiquitin signals autophagic degradation of cytosolic proteins and peroxisomes. *Proc. Natl. Acad. Sci. U.S.A.* 105:20567–20574. doi:10.1073/pnas.0810611105.

Koch, J., K. Pranjic, A. Huber, A. Ellinger, A. Hartig, F. Kragler, and C. Brocard. 2010. PEX11 family members are membrane elongation factors that coordinate peroxisome proliferation and maintenance. *Journal of Cell Science*. 123:3389–3400. doi:10.1242/jcs.064907.

Lach, R.S., C. Qiu, E.Z. Kajbaf, N. Baxter, D. Han, A. Wang, H. Lock, O. Chirikian, B. Pruitt, and M.Z. Wilson. 2022. Nucleation of the destruction complex on the centrosome accelerates degradation of β-catenin and regulates Wnt signal transmission. *Proc. Natl. Acad. Sci. U.S.A.* 119:e2204688119. doi:10.1073/pnas.2204688119.

Levaot, N., O. Voytyuk, I. Dimitriou, F. Sircoulomb, A. Chandrakumar, M. Deckert, P.M. Krzyzanowski, A. Scotter, S. Gu, S. Janmohamed, F. Cong, P.D. Simoncic, Y. Ueki, J. La Rose, and R. Rottapel. 2011. Loss of Tankyrase-Mediated Destruction of 3BP2 Is the Underlying Pathogenic Mechanism of Cherubism. *Cell*. 147:1324–1339. doi:10.1016/j.cell.2011.10.045.

Li, W., Q. Han, Y. Zhu, Y. Zhou, J. Zhang, W. Wu, Y. Li, L. Liu, Y. Qiu, K. Hu, and D. Yin. 2023. SUMOylation of RNF146 results in Axin degradation and activation of Wnt/β-catenin signaling to promote the progression of hepatocellular carcinoma. *Oncogene*. 42:1728–1740. doi:10.1038/s41388-023-02689-4.

Li, X., H. Han, M.-T. Zhou, B. Yang, A.P. Ta, N. Li, J. Chen, and W. Wang. 2017. Proteomic Analysis of the Human Tankyrase Protein Interaction Network Reveals Its Role in Pexophagy. *Cell Reports*. 20:737–749. doi:10.1016/j.celrep.2017.06.077.

Liang, J.R., E. Lingeman, S. Ahmed, and J.E. Corn. 2018. Atlastins remodel the endoplasmic reticulum for selective autophagy. *Journal of Cell Biology*. 217:3354–3367. doi:10.1083/jcb.201804185.

Love, M.I., Huber, W. & Anders, S. Moderated estimation of fold change and dispersion for RNA-seq data with DESeq2. *Genome Biol* **15**, 550 (2014). https://doi.org/10.1186/s13059-014-0550-8

Manner, A., and M. Islinger. 2017. Isolation of Peroxisomes from Rat Liver and Cultured Hepatoma Cells by Density Gradient Centrifugation. In Peroxisomes. M. Schrader, editor. Springer New York, New York, NY. 1–11.

Martino-Echarri, E., M.G. Brocardo, K.M. Mills, and B.R. Henderson. 2016. Tankyrase Inhibitors Stimulate the Ability of Tankyrases to Bind Axin and Drive Assembly of β-Catenin Degradation-Competent Axin Puncta. *PLoS ONE*. 11:e0150484. doi:10.1371/journal.pone.0150484.

Matsumoto, Y., J. Larose, O.A. Kent, M. Lim, A. Changoor, L. Zhang, Y. Storozhuk, X. Mao, M.D. Grynpas, F. Cong, and R. Rottapel. 2017. RANKL coordinates multiple osteoclastogenic pathways by regulating expression of ubiquitin ligase RNF146. *Journal of Clinical Investigation*. 127:1303–1315. doi:10.1172/JCI90527.

Morand, O., L. Allen, R. Zoeller, and C. Raetz. 1990. A rapid selection for animal cell mutants with defective peroxisomes. *Biochimica et Biophysica Acta (BBA) - General Subjects*. 1034:132–141. doi:10.1016/0304-4165(90)90066-6.

Morin, P.J., A.B. Sparks, V. Korinek, N. Barker, H. Clevers, B. Vogelstein, and K.W. Kinzler. 1997. Activation of β-Catenin-Tcf Signaling in Colon Cancer by Mutations in β-Catenin or APC. *Science*. 275:1787–1790. doi:10.1126/science.275.5307.1787.

Morvay, P.L., M. Baes, and P.P. Van Veldhoven. 2017. Differential activities of peroxisomes along the mouse intestinal epithelium. *Cell Biochemistry & Function*. 35:144–155. doi:10.1002/cbf.3255.

Murray, V., J.K. Chen, and A.M. Galea. 2014. The anti-tumor drug bleomycin preferentially cleaves at the transcription start sites of actively transcribed genes in human cells. *Cell. Mol. Life Sci.* 71:1505–1512. doi:10.1007/s00018-013-1456-4.

Nie, L., C. Wang, N. Li, X. Feng, N. Lee, D. Su, M. Tang, F. Yao, and J. Chen. 2020. Proteome-wide Analysis Reveals Substrates of E3 Ligase RNF146 Targeted for Degradation. *Molecular & Cellular Proteomics*. 19:2015–2030. doi:10.1074/mcp.RA120.002290.

Olivieri, M., T. Cho, A. Álvarez-Quilón, K. Li, M.J. Schellenberg, M. Zimmermann, N. Hustedt, S.E. Rossi, S. Adam, H. Melo, A.M. Heijink, G. Sastre-Moreno, N. Moatti, R.K. Szilard, A. McEwan, A.K. Ling, A. Serrano-Benitez, T. Ubhi, S. Feng, J. Pawling, I. Delgado-Sainz, M.W. Ferguson, J.W. Dennis, G.W. Brown, F. Cortés-Ledesma, R.S. Williams, A. Martin, D. Xu, and D. Durocher. 2020. A Genetic Map of the Response to DNA Damage in Human Cells. *Cell*. 182:481-496.e21. doi:10.1016/j.cell.2020.05.040.

Ott, J., J. Sehr, N. Schmidt, W. Schliebs, and R. Erdmann. 2023. Comparison of human PEX knockout cell lines suggests a dual role of PEX1 in peroxisome biogenesis. Biological Chemistry. 404:209–219. doi:10.1515/hsz-2022-0223.

Platta, H.W., F. El Magraoui, B.E. Bäumer, D. Schlee, W. Girzalsky, and R. Erdmann. 2009. Pex2 and Pex12 Function as Protein-Ubiquitin Ligases in Peroxisomal Protein Import. *Molecular and Cellular Biology*. 29:5505–5516. Doi:10.1128/MCB.00388-09.

Platta, H.W., S. Grunau, K. Rosenkranz, W. Girzalsky, and R. Erdmann. 2005. Functional role of the AAA peroxins in dislocation of the cycling PTS1 receptor back to the cytosol. *Nat Cell Biol*. 7:817–822. Doi:10.1038/ncb1281.

Pollock, K., M. Ranes, I. Collins, and S. Guettler. 2017. Identifying and Validating Tankyrase Binders and Substrates: A Candidate Approach. In Poly(ADP-Ribose) Polymerase. A.V. Tulin, editor. Springer New York, New York, NY. 445–473.

Putri, G., Anders, S., Pyl, P., Pimanda, J., Zanini, F., Analysing high-throughput sequencing data in Python with HTSeq 2.0, *Bioinformatics*, Volume 38, Issue 10, May 2022, Pages 2943–2945, https://doi.org/10.1093/bioinformatics/btac166

Schindelin, J., I. Arganda-Carreras, E. Frise, V. Kaynig, M. Longair, T. Pietzsch, S. Preibisch, C. Rueden, S. Saalfeld, B. Schmid, J.-Y. Tinevez, D.J. White, V. Hartenstein, K. Eliceiri, P. Tomancak, and A. Cardona. 2012. Fiji: an open-source platform for biological-image analysis. *Nat Methods*. 9:676–682. doi:10.1038/nmeth.2019.

Sheng, Z., Y. Xu, S. Wang, Y. Yuan, T. Huang, and P. Lu. 2018. XPO1-mediated nuclear export of RNF146 protects from angiotensin II-induced endothelial cellular injury. *Biochemical and Biophysical Research Communications*. 503:1544–1549. Doi:10.1016/j.bbrc.2018.07.077.

Skowyra, M.L., and T.A. Rapoport. 2022. PEX5 translocation into and out of peroxisomes drives matrix protein import. *Molecular Cell*. 82:3209-3225.e7. doi:10.1016/j.molcel.2022.07.004.

Stiebler, A.C., J. Freitag, K.O. Schink, T. Stehlik, B.A.M. Tillmann, J. Ast, and M. Bölker. 2014. Ribosomal Readthrough at a Short UGA Stop Codon Context Triggers Dual Localization of Metabolic Enzymes in Fungi and Animals. *PloS Genet*. 10:e1004685. Doi:10.1371/journal.pgen.1004685.

Stirling, D.R., M.J. Swain-Bowden, A.M. Lucas, A.E. Carpenter, B.A. Cimini, and A. Goodman. 2021. CellProfiler 4: improvements in speed, utility and usability. *BMC Bioinformatics*. 22:433. Doi:10.1186/s12859-021-04344-9.

Thorvaldsen, T.E., N.M. Pedersen, E.M. Wenzel, S.W. Schultz, A. Brech, K. Liestøl, J. Waaler, S. Krauss, and H. Stenmark. 2015. Structure, Dynamics, and Functionality of Tankyrase Inhibitor-Induced Degradasomes. *Molecular Cancer Research*. 13:1487–1501. Doi:10.1158/1541-7786.MCR-15-0125.

Tsukamoto, T., S. Yokota, and Y. Fujiki. 1990. Isolation and characterization of Chinese hamster ovary cell mutants defective in assembly of peroxisomes. *The Journal of cell biology*. 110:651–660. Doi:10.1083/jcb.110.3.651.

Veeman, M.T., D.C. Slusarski, A. Kaykas, S.H. Louie, and R.T. Moon. 2003. Zebrafish Prickle, a Modulator of Noncanonical Wnt/Fz Signaling, Regulates Gastrulation Movements. *Current Biology*. 13:680–685. doi:10.1016/S0960-9822(03)00240-9.

Wanders, R.J.A., and H.R. Waterham. 2006. Biochemistry of Mammalian Peroxisomes Revisited. *Annu. Rev. Biochem.* 75:295–332. Doi:10.1146/annurev.biochem.74.082803.133329.

Wilhelm, L.P., J. Zapata-Muñoz, B. Villarejo-Zori, S. Pellegrin, C.M. Freire, A.M. Toye, P. Boya, and I.G. Ganley. 2022. BNIP3L / NIX regulates both mitophagy and pexophagy. *The EMBO Journal*. 41:e111115. Doi:10.15252/embj.2022111115.

Xu, H., P. Luo, Y. Zhao, M. Zhao, Y. Yang, T. Chen, K. Huo, H. Han, and Z. Fei. 2013. Iduna protects HT22 cells from hydrogen peroxide-induced oxidative stress through interfering poly(ADP-ribose) polymerase-1-induced cell death (parthanatos). *Cellular Signalling*. 25:1018–1026. Doi:10.1016/j.cellsig.2013.01.006.

Xu, Y.-R., M.-L. Shi, Y. Zhang, N. Kong, C. Wang, Y.-F. Xiao, S.-S. Du, Q.-Y. Zhu, and C.-Q. Lei. 2022. Tankyrases inhibit innate antiviral response by PARylating VISA/MAVS and priming it for RNF146-mediated ubiquitination and degradation. *Proc. Natl. Acad. Sci. U.S.A.* 119:e2122805119. Doi:10.1073/pnas.2122805119.

Yagita, Y., Y. Abe, and Y. Fujiki. 2022. De novo formation and maintenance of mammalian peroxisomes in the absence of PEX16. Journal of Cell Science. Jcs.258377. doi:10.1242/jcs.258377.

Yeh, T.-Y.J., K.K. Beiswenger, P. Li, K.E. Bolin, R.M. Lee, T.-S. Tsao, A.N. Murphy, A.L. Hevener, and N.-W. Chi. 2009. Hypermetabolism, Hyperphagia, and Reduced Adiposity in Tankyrase-Deficient Mice. *Diabetes*. 58:2476–2485. Doi:10.2337/db08-1781.

Yue, X., N. Tiwari, L. Zhu, H.D.T. Ngo, J.-M. Lim, B. Gim, S. Jing, Y. Wang, Y. Qian, and I. Lee. 2021. Tankyrase-1-mediated degradation of Golgin45 regulates glycosyltransferase trafficking

and protein glycosylation in Rab2-GTP-dependent manner. *Commun Biol*. 4:1370. Doi:10.1038/s42003-021-02899-0.

Zhang, J., D.N. Tripathi, J. Jing, A. Alexander, J. Kim, R.T. Powell, R. Dere, J. Tait-Mulder, J.-H. Lee, T.T. Paull, R.K. Pandita, V.K. Charaka, T.K. Pandita, M.B. Kastan, and C.L. Walker. 2015. ATM functions at the peroxisome to induce pexophagy in response to ROS. *Nat Cell Biol*. 17:1259–1269. Doi:10.1038/ncb3230.

Zhang, Y., S. Liu, C. Mickanin, Y. Feng, O. Charlat, G.A. Michaud, M. Schirle, X. Shi, M. Hild, A. Bauer, V.E. Myer, P.M. Finan, J.A. Porter, S.-M.A. Huang, and F. Cong. 2011. RNF146 is a poly(ADP-ribose)-directed E3 ligase that regulates axin degradation and Wnt signalling. *Nat Cell Biol*. 13:623–629. Doi:10.1038/ncb2222.

Zheng, J., X. Chen, Q. Liu, G. Zhong, and M. Zhuang. 2022. Ubiquitin ligase MARCH5 localizes to peroxisomes to regulate pexophagy. *Journal of Cell Biology*. 221:e202103156. Doi:10.1083/jcb.202103156.

Zoeller, R.A., and C.R. Raetz. 1986. Isolation of animal cell mutants deficient in plasmalogen biosynthesis and peroxisome assembly. *Proc. Natl. Acad. Sci. U.S.A.* 83:5170–5174. Doi:10.1073/pnas.83.14.5170.

Data Availability

Raw data and count tables from RNAseq (GSE266892) and pooled screen (GSE266855) experiments have been deposited on GEO with the indicated accession numbers. Microscopy images are available from authors upon reasonable request.

Acknowledgements:

We thank Katelynn Kazane for assistance with engineering CRISPRi cell lines. We thank Amos Liang and Jacob Corn for Hct116 CRISPRi cells. We thank Diego Acosta-Alvear for H4 CRISPRi cells. We thank Mary West and Pingping He of the High-Throughput Screening Facility (HTSF) at UC Berkeley for preparation of the pooled CRISPRi library and Jonathan Weissman for the gift of the pooled library. We thank Griffin Kramer with assistance in data processing. We thank members of the Gardner and Richardson labs, Joel Rothman, and Chris Hayes for fruitful discussions. We thank Ron Prywes and Randall Moon for plasmid reagents. Brooke Gardner acknowledges support from K99/R00GM121880, R35GM146784, and the Searle Scholars Program. Jonathan Vu acknowledges support from the Connie Frank Fellowship. Lori Mandjikian acknowledges support from CIRM Educ4. Chris Richardson acknowledges support from R35 GM142975. The content is solely the responsibility of the authors and does not necessarily represent the official views of the National Institutes of Health.

Conflict of Interest Statement:

The authors declare no competing financial interests.

Author Contributions:

J. T. Vu: Conceptualization; Investigation; Formal Analysis; Visualization; Writing – original draft; Writing – review and editing. K. U. Tavasoli: Investigation; Validation. C. J. Sheedy: Investigation; Validation. S. P. Chowdhury: Investigation; Validation. L. Mandjikian: Methodology. J. Bacal: Methodology; Resources. M. A. Morrissey: Resources; Methodology. C. D. Richardson: Conceptualization; Funding Acquisition; Project Administration; Formal Analysis; Supervision; Writing – original draft; Writing – review and editing. B. M. Gardner: Conceptualization; Funding Acquisition; Project Administration; Supervision; Visualization; Writing – original draft; Writing – review and editing

666

667

668

669

Figures

Figure 1. A genome-wide screen uncovers genes that regulate peroxisome biology. (A) Design of the Pex-ZeoR cell line, which sequesters the Zeocin resistance protein in the peroxisome matrix. Loss of PEX genes causes cytosolic Zeocin resistance. **(B)** Representative fluorescence microscopy images of live HCT116 mVenus-ZeoR-PTS1 cells expressing either NTC or PEX1 sgRNAs. Fusion construct forms puncta in WT but not aperoxisomal (PEX1 knockdown) cells. Fluorescent microscopy data are representative of n=49 images from m=2 biological replicates. Scale bar: 10μm **(C)** Quantification of flow cytometry data of BFP- (NTC) and BFP+ (PEX1) cells grown in co-culture competition assay over t=11 days in the presence of 0, 25, or 50 ng/uL of Zeocin. Timepoints are taken every t=2 days. Data shown as the mean ± SD of n=3 biological replicates. **(D)** Volcano plot of NGS data from genome-wide screen with significance (-log base 10 of p-value, y-axis) and phenotype score (normalized fold change of cDNA guide count, x-axis) of guides targeting specific genes for cell cultures either untreated (DMSO mock treated) or treated (50ng/uL Zeocin treated) for 14 days. Red data points represent known PEX genes and HIF1A. The green data point represents RNF146. Data displayed was calculated from m=3 guides per gene and n=2 biological replicates.

Figure 2. Peroxisome abundance is regulated locally by RNF146. (A) CellProfiler quantification of the ratio of mVenus-PTS1 intensity in foci and in the cytoplasm in fluorescence microscopy images acquired of live HCT116 Pex-ZeoR cells expressing sgRNAs targeting various genes. Data per gene constitutes m=2 unique sgRNAs with n=49 images per gene. Non-targeting control sgRNA shown in yellow, PEX1 sgRNA shown in pink, sgRNAs significantly different from NTC ($p<0.0001$, independent t-test) are in blue, sgRNA with $p>0.05$ are in white. **(B)** Representative fluorescence microscopy images of mVenus expression in HCT116 Pex-ZeoR cells harboring sgRNAs for NTC, PEX1, or RNF146 and quantification of the ratio of mVenus-PTS1 foci intensity to mVenus-PTS1 cytosolic intensity. Data is representative of m= 49 images. n=2 biological replicates. Scale bars: 10 μm. **(C)** Representative fluorescence microscopy images of mVenus expression in HCT116 Pex-ZeoR cells treated with either scrambled (scr) siRNA or RNF146 siRNA, and quantification of the ratio of total mVenus-PTS1 foci intensity to mVenus-PTS1 cytosolic intensity. Data is representative of m= 49 images n=2 biological replicates. Scale bar: 10 μm. **(D)** Representative fluorescence microscopy images of mVenus expression in H4 Pex-ZeoR cells harboring sgRNAs for NTC, PEX1, or RNF146 and quantification of the ratio of mVenus-PTS1 foci intensity to mVenus-PTS1 cytosolic intensity. Data is representative of m= 49 images. n=2 biological replicates. Scale bars: 10μm. Asterisks denote ****$p<0.0001$. **(E)** Heatmap of RNA-seq data displaying significant ($p<0.05$) fold change of *PEX* gene transcription in RNF146 knockdown cells versus NTC controls. Data is representative of n=3 biological replicates.

Figure 3. RNF146's effect on peroxisomes is mediated by TNKS/2, but not autophagy. (A) Immunoblots for TNKS/2 and ACTB (loading control) in lysate from scrambled or TNKS/2 siRNA treated HCT116 Pex-ZeoR cells with sgRNAs for either NTC or RNF146. **(B)** Left panel: Representative mVenus-PTS1 fluorescence microscopy images of either non-targeting control (NTC) or RNF146 sgRNA cells treated with either scrambled (scr) siRNA or TNKS siRNA. Right panel: Quantification of mVenus-PTS1 microscopy images in left panel for mVenus-PTS1 foci intensity versus total cytosol intensity in HCT116 Pex-ZeoR cells. Data is representative of 49 images per condition and 2 biological replicates. Scale bars: 10 μm. **(C)** Immunoblot for TNKS/2, ATG7, and LC3B in lysate from scrambled or ATG7 siRNA treated HCT116 Pex-ZeoR cells with sgRNAs for either NTC or RNF146. **(D)** Left panel: Fluorescence microscopy data of scrambled or ATG7 siRNA treated HCT116 Pex-ZeoR cells with sgRNAs for either non-targeting control (NTC) or RNF146. m=32 images. n=2 biological replicates. Right panel:

Quantification of mVenus-PTS1 microscopy images for mVenus foci intensity versus cytosol intensity in HCT116 Pex-ZeoR cells. Scale bars: 10μm. All blots are representative of n=3 biological replicates. Asterisks denote p-values *p <0.05, ****p <0.0001, whereas ns denotes not significant, calculated by independent t-test.

Figure 4. Loss of RNF146 impairs peroxisome protein import. (A) Representative immunofluorescence microscopy images of NTC, RNF146, PEX19, and PEX5 sgRNA expressing HCT116 Pex-ZeoR cells. mVenus-PTS1 in green, DAPI in blue, PMP70 in magenta. **(B, C)** Quantification of immunofluorescence microscopy images for percentage foci area of PMP70 (B) and mVenus-PTS1 (C) versus cytosolic area. m=25 images. n=2 biological replicates. Asterisks denote p-values **p <0.01, ***p <0.001, ****p <0.0001, whereas ns denotes not significant, calculated by independent t-test. **(D)** Immunoblot of HCT116 Pex-ZeoR with sgRNAs targeting NTC, RNF146, and PEX5. Fractions represent total lysate (T), 20,000xg supernatant (S), and 20,000xg pellet (P). Densitometry quantification of blots represents the normalized (to NTC) fold change of the densitometric ratio of soluble vs. pellet fractions (R=S/P) of selected proteins. Triangle for anti-PEX14 blot denotes the band that disappears with PEX14 sgRNA treatment. All blots are representative of n=3 biological replicates.

Figure 5. TNKS/2 PARP activity impairs peroxisome protein import. (A) Immunoblots of anti-TNKS/2 immunoprecipitation fractions from HCT116 Pex-ZeoR cells expressing PEX14 sgRNAs with constitutive re-expression for FLAG-PEX14 treated with either NTC or RNF146 siRNA (10 nM) for 24hrs, detecting TNKS/2, PEX5, and PEX14. **(B)** Representative live-cell fluorescence microscopy images of NTC and RNF146 sgRNA expressing HCT116 Pex-ZeoR cells treated with DMSO (mock), 500 nM G007LK, or 10 μM XAV939 for 24 hrs. mVenus-PTS1 in green. Scale bar: 10 μm. **(C)** Quantification of fluorescence microscopy images for the ratio of mVenus-PTS1 foci intensity to mVenus-PTS1 cytosolic intensity (left) and the number of foci per cell (right). m=32 images and n=2 biological replicates. Asterisks denote p-values *p <0.05, **p <0.01, ***p <0.001, ****p <0.0001, whereas ns denotes not significant, calculated by independent t-test. (**D**) Immunoblots of anti-FLAG immunoprecipitation Total Lysate (input) and Elution fractions from HCT116 Pex-ZeoR cells expressing NTC sgRNA (lane 4/8) or PEX14 sgRNAs with constitutive re-expression for PEX14-FLAG (lane 1/2/3/5/6/7) treated with either NTC or RNF146 siRNA (10 nM) for 24hrs, with or without XAV939 (1 μM) for 24hrs., and with carfilzomib (10 μM) for 4hrs, detecting FLAG, Poly-(ADP)-ribose (PAR),TNKS/2, PEX5, PEX13, and PEX14. Representative of n=2 biological replicates. **(E)** Immunoblots of lysates from HCT116 CRISPRi cells harboring NTC guides treated with either NTC or RNF146 siRNA (10 nM) for 48 hrs, and with or without XAV939 (1 μM) for 24hrs. Representative of n=4 biological replicates. (**F**) Proposed model: loss of RNF146 increases active TNKS/2, which binds PEX14 and PARsylates proteins at the peroxisome membrane impairing peroxisome import.

Figure 6. Peroxisome abundance influences RNF146/TNKS substrate selection. (A-C) Immunoblots measuring the abundance of AXIN1, CASC3, and BLZF in **(A)** HCT116 (n=3), **(B)** HEK293 (n=3), and **(C)** iPSC AICS-0090-391 (n=3) CRISPRi cells with indicated sgRNAs. **(D)** Western blot measuring abundance of AXIN1 and ACTB (loading control) in HCT116 cells with indicated sgRNAs, PEX19 knockdown cells are paired with treatments for PEX19 reexpression, TNKS siRNA (10 nM), RNF146 siRNA 10 nM), or XAV939 (10 μM). Blots shown are representative of n=1 blots. **(E-F)** TOPFlash Dual Luciferase assays measuring the induction of Wnt signaling to downstream beta-catenin transcription in PEX knockdown HCT116 cells (E) and HEK293T (F) harboring the indicated sgRNAs and treated with or without 315ng/mL Wnt3a for 24 hrs (data shown is 48 hours post-transfection with TOPFlash constructs). Luciferase activity is measured versus a Renilla transfection control and data is normalized to untreated NTC samples. FOPFlash negative control performed in NTC sgRNA cells. Data is

766 representative of n=3 biological samples. Asterisks denote p-values *p <0.05, **p <0.01,
767 calculated by paired t-test.

768

Materials and Methods

Cell Lines, Culture Conditions, Lentiviral Production and Transduction

H4 dCas9-KRAB (a gift from the laboratory of Diego Acosta-Alvear, UCSB), HEK293T, and HCT116 dCas9-KRAB (a gift from the laboratory of J. Corn, ETH Zürich) cells were cultured in Dulbecco's Modified Eagle Media (10565018, DMEM, Gibco) supplemented with 10% fetal bovine serum (FBS, S11150H, R&D Systems), 1% penicillin/streptomycin (15140122, Gibco), and 2 mM L-Glutamine, and kept at 37°C and 5% CO_2 in a humidified incubator. Generation of lentivirus was performed by transfecting HEK293T cells with standard delta VPR and VSVG packaging vectors paired with TransIT-LTI Transfection Reagent (MIR2305, Mirus). Lentivirus was harvested 72 hrs following transfection and frozen at -80°C.

Zeocin resistance harboring HCT116 CRISPRi cell lines were constructed by transducing cells with lentivirus expressing mVenus-ZeoR-PTS1 constructs with either a PGK (pCR2054) or hEF-1α (pCR2055) promoter and 'spinfecting' cells in a centrifuge at 1000 rpm for 2 hrs. ZeoR expressing cells were single-cell sorted by flow cytometry (Sony SH800S) for mVenus expression at 488 nm excitation, where modestly fluorescent monoclonal cells were selected for both promoter types.

Re-expression constructs were made by Gibson cloning desired CDS sequences into the pLentiX-CD90 Thy1.1 vector backbone, with subsequent cell sorting of Thy1.1 positive cells by immunolabeling with CD90.1 Thy-1.1 antibody (17-0900-82, Thermo Scientific).

For drug treatment conditions, cells were treated with 50 nM bafilomycin (B1793, Sigma-Aldrich) for 15 hours, 5-10 µM hydroxychloroquine (H0915, Sigma-Aldrich) for 24 hours, 500 nM G007-LK (S7239, Selleck) for 24 hours, 1 µM XAV939 (575545, EMD Millipore) for 24 hours, and Carfilzomib (PR-171, Selleck) 10 µM for 4 hours.

For siRNA treatment conditions, cells were transfected with 10 nM of desired siRNA using Lipofectamine RNAiMAX (13778150, ThermoFisher) according to the manufacturer's protocol for 24-48 hrs.

A list of siRNA and sgRNA sequences used in the manuscript is available in **Table S3.**

iPS cells

AICS-0090-391 (WTC-CLYBL-dCas9-TagBFP-KRAB-cl391) cells were cultured in 10 ml sterile-filtered mTeSR-Plus (100-0276, STEMCELL) on a Matrigel-coated plate (354277, Corning) and grown to 80% confluency, five days post-thaw at 37°C and 5% CO2 in a humidified incubator. For routine passaging, at 80% confluency, media was aspirated and cells were washed with 4 ml room temp DPBS prior to dissociation. iPSCs were then treated with 2 ml pre-warmed Accutase (AT104, Stem Cell Technologies) and the vessel was incubated at 37ºC for 10 mins. Once cells began to detach, 4 mLs DMEM/F12 were added to the Accutase-treated cells and dissociated cells were triturated. Cells were rinsed with an additional 7 ml of DPBS for a final wash, and the dissociated cell suspension was transferred to a 15 ml conical tube and centrifuged at 500g for 5 min at room temp. DMEM/F12/Accutase supernatant was carefully aspirated and cells were resuspended in 10 ml fresh mTeSR-Plus containing 10µM Y-27632 2HCl (ROCK Inhibitor, S1049, Selleck) (ROCKi) and counted via flow cytometry. Cells were then seeded into a Matrigel-coated six-well dish at a density of 1.5e+05 per well in 3 ml mTeSR-Plus containing ROCKi. Old media containing ROCKi was aspirated from each well the next day

and replaced with fresh mTeSR1 without ROCKi. mTeSR-Plus was changed daily, and ROCKi was used for each passaging event, and always removed 24 hours thereafter.

Genome-wide Pooled CRISPRi Screen and Analysis

HCT116 CRISPRi pCR2054 cells were transduced with lentivirus harboring constructs expressing sgRNAs from the genome-wide pooled CRISPRi v2 library with 8µg/mL of polybrene (TR-1003-G, EMD Millipore) at a multiplicity of infection (MOI) of <1. hCRISPRi-v2 library was a gift from Jonathan Weissman (Addgene ID #83969). Cells were then selected with 1.5 µg/mL puromycin (A1113803, Gibco) for 1 week in 15 cm dishes and expanded to 3.60 x 10^8 cells to allow for T0 condition takedowns as well as base seed for Zeocin (R25001, Invitrogen) treated and untreated samples. Treated cells were subjected to Zeocin 25 ng/µL final concentration and untreated cells were substituted with DMSO. Cells were maintained at >500X coverage per library element per replicate per condition throughout the screen. Cells were then cultured for 35 days in 5-Chamber CellStack vessels, splitting cells every 48-72hrs. and harvesting 2.40 x 10^8 cells every 7 days per condition, where the treated and untreated conditions reached ~8 and ~16 doublings at day 14, respectively. Genomic DNA was purified using Macherey-Nagel NucleoSpin Blood XL Maxi Kit (740950.50, Macherey-Nagel) and prepared as previously described [Kampmann et al 2014] with modifications: Sbf1 (R3642S, NEB) was used instead of PvuII for the restriction digest. Next-Generation Sequencing (NGS) was performed using an Illumina NovaSeq SP with 2x50 paired end reads using custom read primers:
Read 1:
GTGTGTTTTGAGACTATAAGTATCCCTTGGAGAACCACCTTGTTGG
Read 2:
CTAGCCTTATTTAAACTTGCTATGCTGTTTCCAGCTTAGCTCTTAAAC
NGS data was then quantified and phenotype scores were generated using python scripts from the Horlbeck Lab's ScreenProcessing pipeline as previously described [Horlbeck et al 2016].

Immunofluorescence Staining

Cells were plated on glass bottom 96-well plates and fixed using 4% paraformaldehyde (15710, Electron Microscopy Sciences) in DPBS (14190250, Gibco) for 10 minutes and washed twice with DPBS. Cells were then permeabilized using 0.25% Triton X-100 (A16046.AP, Thermo Fisher) in DPBS for 10 minutes, blocked with 3% BSA (BP9703100, Fisher Scientific) in PBST (DPBS, Gibco; 0.1% Tween 20, AAJ20605AP, Thermo Fisher) for 30 minutes, and then probed with desired antibody in 3% BSA PBST for 1 hour at RT. Cells were then washed 3 times with PBST and incubated with secondary antibody and DAPI (D1306, Invitrogen) in 3% BSA PBST for 1 hour at RT in darkness. Cells were then washed 3 times in PBST and stored in DPBS prior to image acquisition.

A list of antibodies used in the manuscript is available in **Table S4.**

Confocal Microscopy and Analysis

Fluorescent image acquisition was performed using a Nikon Eclipse Ti2 configured with a spinning disk confocal scanner (Yokogawa, CSU-W1), CFI Plan Apochromat Lambda D 40X air objective lens, CFI Apochromat TIRF 100X/1.49 oil-immersion objective lens, and NIS-Elements AR software (Nikon, version 5.31.01). Green (mVenus), blue (BFP, DAPI), red, and far red were excited with 488, 405, 561, and 640 nm lasers, respectively. Microscopy images were post-processed using ImageJ/FIJI software (version 2.0.0). Quantification and analysis of microscopy images was performed using CellProfiler [Stirling et al 2021] (version 4.2.4). For live cell images, acquired images were thresholded by global minimum cross entropy to select for and differentiate between cell cytoplasm area and mVenus foci area in an unbiased manner; downstream mVenus foci number, area, and intensity was measured within a range of size and

ROI. For immunofluorescence microscopy, images were processed by, first, defining nuclei stained by DAPI by adaptive Otsu 3-class thresholding to differentiate between background and nuclei; second, by expanding from nuclei objects to define cytoplasm based on distance and Otsu 2-class thresholding and then subtracting nuclei from this area; third, by selecting, within the cytoplasm area, foci objects for mVenus, Catalase, or PMP70 of a defined size and ROI determined by adaptive Otsu 3-class thresholding. All of the previously mentioned objects are then measured for number, area, intensity, and colocalization by Pearson's correlation.

Fluorescence-activated Cell Sorting

Flow cytometry was performed using an Attune NxT Flow Cytometer (Invitrogen) or SH800S (Sony). Excitation wavelengths of 488 nm (530/30 filter) and 405 nm (450/40 filter) were used to analyze mVenus and BFP expression, respectively. For selection of cells re-expressing PEX14 or PEX19, cells were sorted for Thy1.1 positive cells after immunolabeling with APC-conjugated CD90.1 Thy-1.1 antibody (17-0900-82, Thermo Scientific) at excitation wavelength of 638 nm (720/60 filter). FCS data was analyzed and visualized using FlowJo (version 10.6.2).

Immunoblotting

Cells were trypsinized (0.05% Trypsin, 25300062, Gibco), quenched, spun down at 300 x g for 5 minutes, decanted, and washed using DPBS (14190250, Gibco). Cells were lysed using RIPA lysis buffer (0.1% SDS, BP8200100, Fisher Scientific, 1% IPEGAL CA630, 8896, EMD-Millipore; 0.5% sodium deoxycholate, D6750, Sigma, 50mM Tris, BP152-5, Fisher Scientific; 150mM NaCl, S271-10, Fisher Scientific) with benzonase (101697, EMD Millipore) and protease inhibitor (78430, Thermo Scientific) for 30 minutes on ice and spun down at 14,000 rpm for 5 minutes and supernatant collected. Total protein concentrations were quantified using Bio-Rad Protein Assay (5000006, Bio-Rad). Protein samples were normalized to 10-20 µg, mixed with 4X Laemmli sample buffer (62.5mM Tris, 10% glycerol, 1%SDS, 0.005% bromophenol blue) containing beta-mercaptoethanol (M6250, Sigma-Aldrich), and incubated for 5 minutes at 95 deg C. Samples were loaded and resolved on 4-20% SDS-PAGE gels (#4561095, Bio-Rad), semi-dry transferred to 0.45 µm LF PVDF membranes (1620264, Bio-Rad), blocked in 5% milk (Nestle) in TBST (50mM Tris, 150mM NaCl, pH 7.4), and probed with desired antibody in 3% BSA TBST (BSA, BP9703100, Fisher Scientific) overnight at 4C. Membranes were then washed and probed with secondary HRP-conjugated antibodies, with visualization of chemiluminescence using Pierce ECL2 Western Blotting Substrate (PI80196, Thermo Scientific) on a ChemiDoc MP Imaging System (Bio-Rad). Densitometry was performed using Fiji [Schindelin et al 2012].

TOPFlash

HEK293T ZIM3-dCas9 and HCT116 dCas9-KRAB cells harboring NTC, PEX14, and PEX19 sgRNAs were transfected in 96-well plates by lipofectamine (TransIT LT-1, Mirus). A normalized 55 ng of total plasmid DNA was used at a ratio of 50:5 TOPFlash/FOPFlash:Renilla. Cells were treated with either BSA or human recombinant WNT3a (5036-WN-010, R&D Systems) 24 hours later. Cells were then lysed 24 hours after treatment and luciferase activity was measured using the Dual Luciferase Assay (E1910, Promega) according to manufacturer's protocol, and luminosity was read out using a microplate reader (SpectraMax M5, Molecular Devices). Plasmids used were: TopFLASH (Addgene#12456), FopFLASH (Addgene#12457), Renilla (Addgene#27163). M50 Super 8x TOPFlash and M51 Super 8x FOPFlash (TOPFlash mutant) were a gift from Randall Moon (Addgene plasmid # 12456, #12457) [Veeman et al 2003]. pRL-SV40P was a gift from Ron Prywes (Addgene plasmid # 27163) [Chen and Prywes 1999].

Subcellular Fractionation

Designated cell lines were harvested at 25-30 million cells (equalized among experimental

replicates), spun down, washed, and resuspended in Homogenization Buffer (HB) (250 mM sucrose, 5 mM MOPS, 1 mM EDTA, 2 mM PMSF, 1 mM DTT, 1 mM ε-aminocaproic acid, pH 7.4 adjusted with KOH) based on Manner and Islinger et al. 2018. Cells were quickly freeze thawed and mechanically homogenized via dounce, with a minimum of 10 passes, to lyse the extracellular membrane while retaining intracellular organelles. Total lysate was collected. The remainder of the product was centrifuged at 600 × g max, 10 min, 4 °C, the supernatant collected, pellet was then collected and resuspended with HB, homogenized via dounce, with a minimum of 10 passes again, centrifuged at 600 × g max, 10 min, 4 °C, supernatant collected and combined with previously collected supernatant, whereas the remaining pellet is considered the nuclear pellet. The supernatant was then fractionated at 20,000xg for 30 minutes at 4°C. The fractionated supernatant was harvested (cytoplasmic fraction), leaving behind the heavy mitochondrial/light mitochondrial/peroxisomal organellar pellet. The pellet is washed by resuspension in 1 mL of homogenization buffer, spun down at 20,000xg for 15 minutes at 4°C, the wash supernatant is discarded, and then washed again in the same manner. The resulting organellar pellet is lysed by RIPA lysis buffer; this is considered the cell pellet.

Co-Immunoprecipitation

Designated cell lines were harvested at 10-15 million cells (equalized among experimental replicates), spun down, and resuspended in LB1 (60 mM HEPES pH 7.6, 150 mM NaCl, 150 mM KCl, 10 mM MgCl2, 0.2% IPEGAL CA630 (Sigma), 0.1% sodium deoxycholate (Sigma), 1X Protease Inhibitor, with or without 1X Benzonase). For FLAG-IP assaying for PARsylation: no benzonase, 1 µM PARGi, and 10 µM carfilzomib was included in the LB1. The suspension quickly undergoes freeze-thaw, is then dounce homogenized (with a minimum of 10 passes), and then is incubated for 30 minutes at 4°C with inversion. Total lysate samples are acquired and the remaining lysate is centrifuged for 5 min, 20,000xg at 4°C to separate the sample into soluble and insoluble fractions. The supernatant (soluble fraction) is collected and spun at 20,000 xg at 4°C for 30 minutes to clear out any remaining insoluble proteins or cell debris, this is the lysate supernatant. The insoluble fraction is washed with LB1, spun down, decanted, and resuspended in LB1, this is the pellet. In an optional step, the lysate supernatant is pre-cleared with protein G agarose beads for 30 minutes at 4°C and washed. For FLAG-IPs, supernatant is incubated with M2 FLAG conjugated agarose beads (M8823, Millipore) for 2-3 hrs at 4°C with inversion. For TNKS immunoprecipitations, supernatant is incubated with 10 µg of TNKS antibody (sc-365897, Santa Cruz Biotech) for 3 hrs at 4°C with inversion, and then conjugated to Protein G Dynabeads (10004D, Invitrogen) for 3hrs. at 4°C with inversion. Beads are then washed 5X in LB2 buffer (LB1 buffer without protease inhibitors or benzonase) with either centrifugation or magnetic stand (where applicable). Beads are then eluted using 50 µL of freshly prepared (day of) Elution Buffer (100 mM NaHCO3, 1% SDS) at 65°C for 15 min on a heated shaker (1200 rpm) twice, or for FLAG-IP assaying for PARsylation, 90ul of 300ug/ml FLAG peptide is dissolved in LB2, and samples are eluted at 4°C shaking at 1100rpm for 30 minutes, then spun down, and supernatant is collected.

RNA-Seq

HCT116 Pex-ZeoR cell lines harboring either NTC or RNF146 sgRNAs were harvested, spun down, and RNA was extracted using RNeasy Mini Kit (Qiagen #74104) according to manufacturer instructions, in triplicate. Purified RNA samples were poly-(A) enriched, reverse transcribed, and sequenced on an Illumina NovaSeq to produce paired-end 150 bp reads (Novogene). Raw fastq reads were trimmed using fastp v0.23.2 [Chen et al. 2018], alignment was done via STAR v 2.7.11a [Dobin et al. 2013], count tables were generated using htseq2 v. 2.0.2 [Putri et al. 2022] and differential expression analysis was performed using the R-package DESeq2 v. 1.40.1 [Love et al. 2014]. Differential expression comparisons were made between experimental and nontargeting CRISPRi strains in biological triplicate.

972

List of Supplementary Materials:

Figures S1 to S5
Table S1 to S4

Figure S1. (A) Quantification of cell count by flow cytometry in different concentrations of Zeocin of HCT116 cells with sgRNAs targeting NTC, PEX1, or PEX6, over 72 hrs. Data is representative of n=2 biological replicates. Cell count is normalized to untreated. **(B)** Quantification of flow cytometry data of BFP- (NTC) and BFP+ (PEX6) cells grown in co-culture competition assay over t=11 days in the presence of 0, 25, or 50 ng/uL of Zeocin. Timepoints are taken every t=2 days. Data shown as the mean ± SD of n=3 biological replicates. **(C)** Schematic of the CRISPRi screen. Pex-ZeoR cells were transformed with a genome-wide gRNA library, selected for expression of guides, and split into untreated and +Zeocin growth conditions. Genomic DNA takedowns for NGS sequencing at t=0 and t=7x for all conditions. **(D)** Heatmap showing Pearson's correlation coefficient of guide abundance for all library elements between biological replicates of sequenced timepoints between treated and untreated conditions. T and Z represent untreated and Zeocin treated conditions, respectively, while numbers represent timepoint (days). Highlighting indicates comparisons between day 14 samples. **(E)** Fold change of various PEX sgRNA abundances derived from genome-wide CRISPRi screen comparing Zeocin treated to untreated samples. Highlighting indicates comparisons between day 14 samples. Y-axis is phenotype score, a measure of fold change of 3 of 5 significant guides per gene. X-axis is time (t) in days. Data is representative of n=2 biological samples. **(F)** Volcano plot of NGS data from genome-wide screen with significance (-log base 10 of p-value, y-axis) and phenotype score (normalized fold change of cDNA guide count, x-axis) of guides targeting specific genes for cell cultures either untreated (DMSO mock treated) or treated (50ng/uL Zeocin treated) for 14 days. Pink data points are output genes filtered through the Olivieri et al. Bleomycin screen that also have p-value <.05 and minimum phenotype score of 1. Gray data points are genes that did not pass filter. Red data points represent known PEX genes and RNF146. Data displayed was calculated from m=3 guides per gene and n=2 biological replicates.

Supplementary Figure 2. (A)(B) Additional data as in Figure 2A CellProfiler quantification of the ratio of mVenus-PTS1 intensity in foci and in the cytoplasm in fluorescence microscopy images acquired of live HCT116 Pex-ZeoR cells expressing sgRNAs targeting various genes. **(A)** Positive phenotype score genes from the primary genetic screen. **(B)** Negative phenotype score genes from the primary genetic screen. Data per gene constitutes m=2 unique sgRNAs with n=49 images per gene. Non-targeting control sgRNA shown in yellow, PEX1 sgRNA shown in pink, sgRNAs significantly different from NTC are in blue ($p<0.0001$, independent t-test) or purple ($p<0.05$, independent t-test), and sgRNAs with $p>0.05$ are in white.

Figure S3. (A) Left Panel: Representative fluorescence microscopy images of NTC, RNF146, TNKS sgRNA expressing HCT116 Pex-ZeoR cells treated with either scrambled siRNA (scRNA), RNF146 siRNA, or TNKS/2 siRNA (10 μM) for 24 hrs. X represents no sample/image. Scale bar: 10 μm. Right Panel: Quantification of mVenus-PTS1 microscopy images in left panel for mVenus foci intensity (peroxisomes) versus total cytosol intensity. Data is representative of m=32 images per condition and n=2 biological replicates. **(B)** Left Panel: Representative immunofluorescence microscopy images of NTC and RNF146 sgRNA expressing HCT116 Pex-ZeoR cells treated with DMSO (mock) or 50 nM Bafilomycin A1 (Baf) for 15 hrs. mVenus-PTS1 in green, DAPI in blue, and PMP70 in cyan. Scale bar: 10 μm. Right panel: Quantification of percentage foci area of mVenus-PTS1 and PMP70 versus cytosolic area for m=21 images and n=2 biological replicates. **(C)** Immunoblot of TNKS and LC3B of cell lysate from conditions in B.

(D) Left Panel: Representative immunofluorescence microscopy images of NTC and RNF146 sgRNA expressing HCT116 Pex-ZeoR cells treated with DMSO (mock), 5 µM hydroxychloroquine (HCQ), or 10 µM hydroxychloroquine for 24hrs (5 µM HCQ not shown). mVenus-PTS1 in green, PMP70 in magenta, and DAPI in blue. Scale bar: 10µm. Right panels: Quantification of immunofluorescence microscopy images for percentage foci area of mVenus and PMP70, respectively, versus cytosolic area. for m=32 images and n=2 biological replicates. **(E)** Immunoblots of cellular lysate from (D) against TNKS/2 and LC3B. **(F)** Left Panel: Representative fluorescence microscopy images of NTC and RNF146 sgRNA expressing H4 Pex-ZeoR cells treated with DMSO (mock) or 50 nM Bafilomycin A1 for 15 hrs. Scale bar: 10 µm. Right panel: Quantification of mVenus-PTS1 microscopy images in left panel for mVenus foci intensity (peroxisomes) versus total cytosol intensity. Data is representative of m=32 images per condition and n=2 biological replicates. (**G**) Immunoblots of cellular lysate from left panel against TNKS and LC3B. All immunoblots are representative of n=3 independent blots. Asterisks denote p-values *p <0.05, **p <0.01, ***p <0.001, ****p <0.0001, whereas ns denotes not significant, calculated by independent t-test.

Figure S4. (A) Left Panel: Representative immunofluorescence microscopy images of NTC, RNF146, PEX19, and PEX5 sgRNA expressing H4 Pex-ZeoR cells. mVenus-PTS1 in green, DAPI in blue, PMP70 in magenta. **(B, C)** Quantification of immunofluorescence microscopy images for percentage foci area of PMP70 **(B)** and mVenus **(C)**, respectively, versus cytosolic area. n=25 images. **(D)** Left Panel: Representative immunofluorescence microscopy images NTC, RNF146, PEX19, and PEX5 sgRNA expressing cells. Catalase in yellow, DAPI in blue, PMP70 in magenta. m=25 images. n=2 biological replicates. Right panel: Quantification of Pearson's correlation coefficient of catalase and PMP70 colocalization of microscopy images. (E) Left Panel: Schematic showing the predicted TBMs of PEX14 with amino acid positions, compared to the predicted consensus TBMs of Guettler et al. 2016 and Pollock et al. 2017. Red=essential, dark orange=common/variable, light orange=variable, yellow=uncommon/accepted, grey=no pattern, G*= glycine or small non hydrophobic, D*= D/E with some variability, defaced P= no proline. Star = Chosen ΔTBM. Right Panel: Immunoblots of anti-FLAG immunoprecipitation total and elution fractions from HCT116 Pex-ZeoR cells expressing PEX14 sgRNAs with constitutive re-expression of either FLAG-PEX14 (WT) or FLAG-PEX14-ΔTBM3 (ΔT), treated with either NTC or RNF146 siRNA (10 nM) for 24hrs, detecting TNKS/2, PEX5, and PEX14. Blots are representative of n=3 biological replicates.

Figure S5. (A) Immunoblot measuring the abundance of AXIN1 in H4 CRISPRi cells expressing sgRNA for NTC, PEX5, PEX14, PEX19, and RNF146.

Figure 1

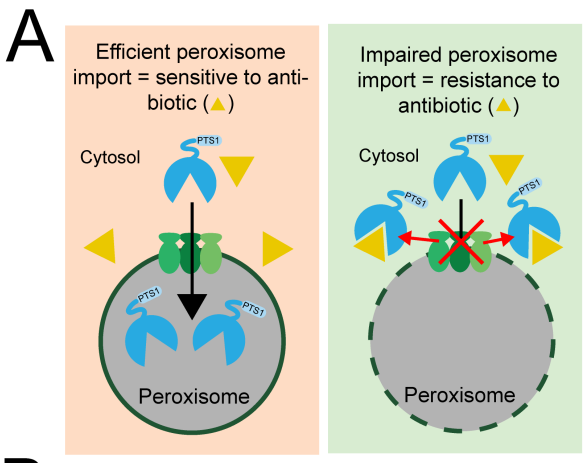
A
Efficient peroxisome import = sensitive to anti-biotic (▲)
Cytosol
PTS1
Peroxisome
Impaired peroxisome import = resistance to antibiotic (▲)
Cytosol
PTS1
Peroxisome

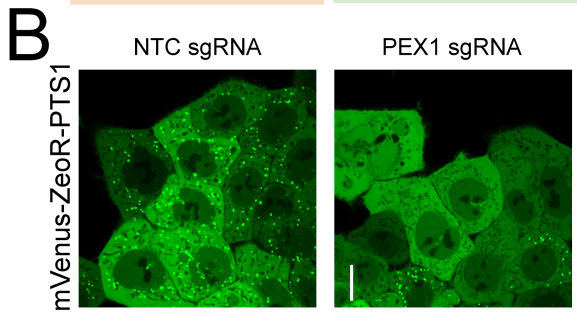
B
NTC sgRNA
PEX1 sgRNA
mVenus-ZeoR-PTS1

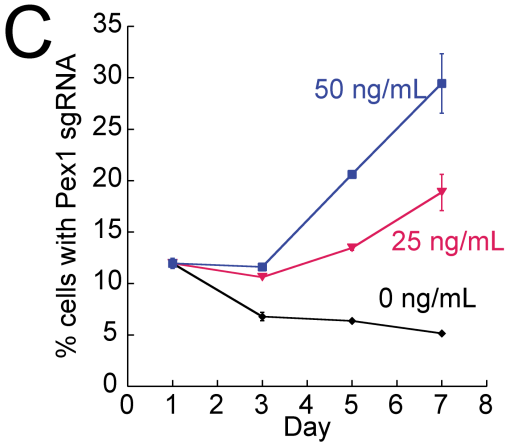
C
% cells with Pex1 sgRNA
Day
50 ng/mL
25 ng/mL
0 ng/mL

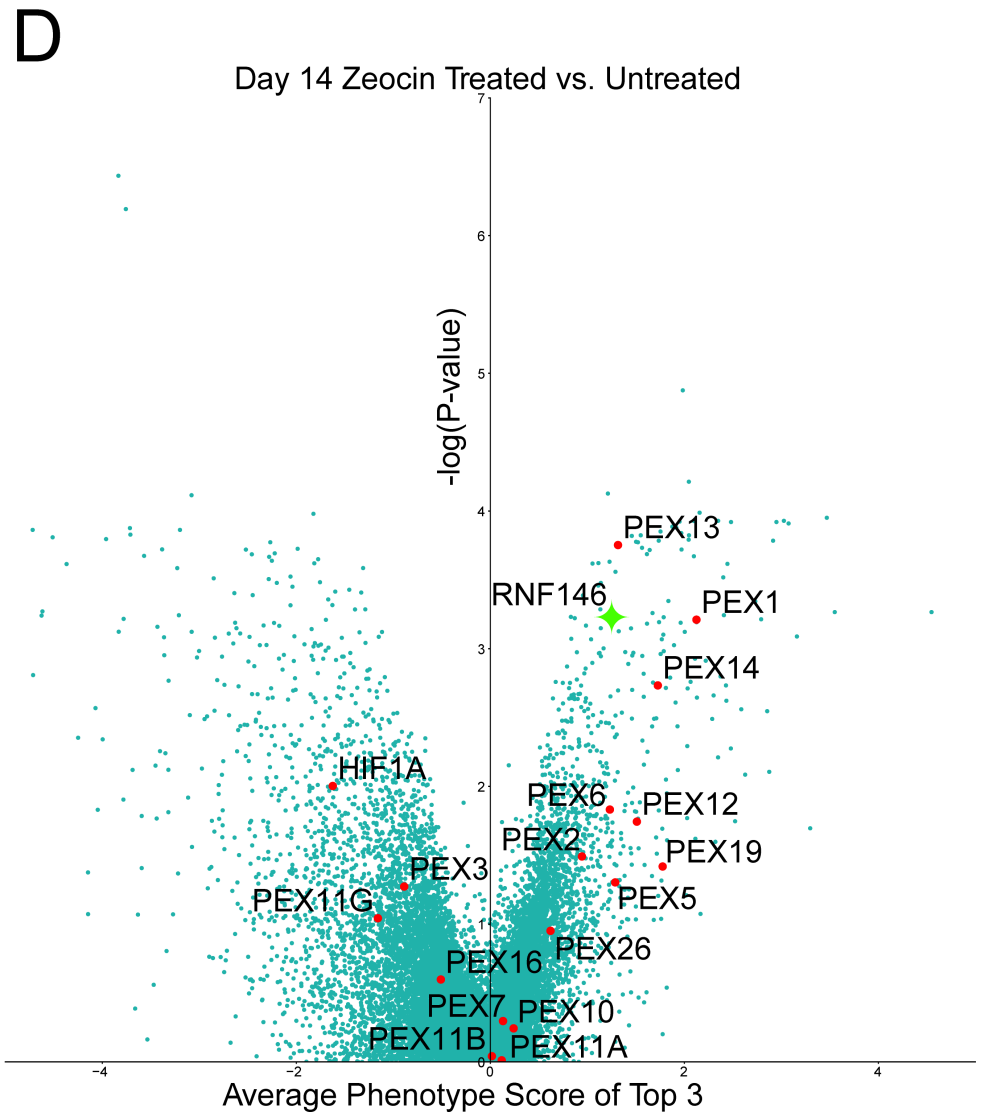
D
Day 14 Zeocin Treated vs. Untreated
-log(P-value)
Average Phenotype Score of Top 3
PEX13
RNF146
PEX1
PEX14
HIF1A
PEX6
PEX12
PEX2
PEX19
PEX3
PEX5
PEX11G
PEX26
PEX16
PEX7
PEX10
PEX11B
PEX11A

Figure 2

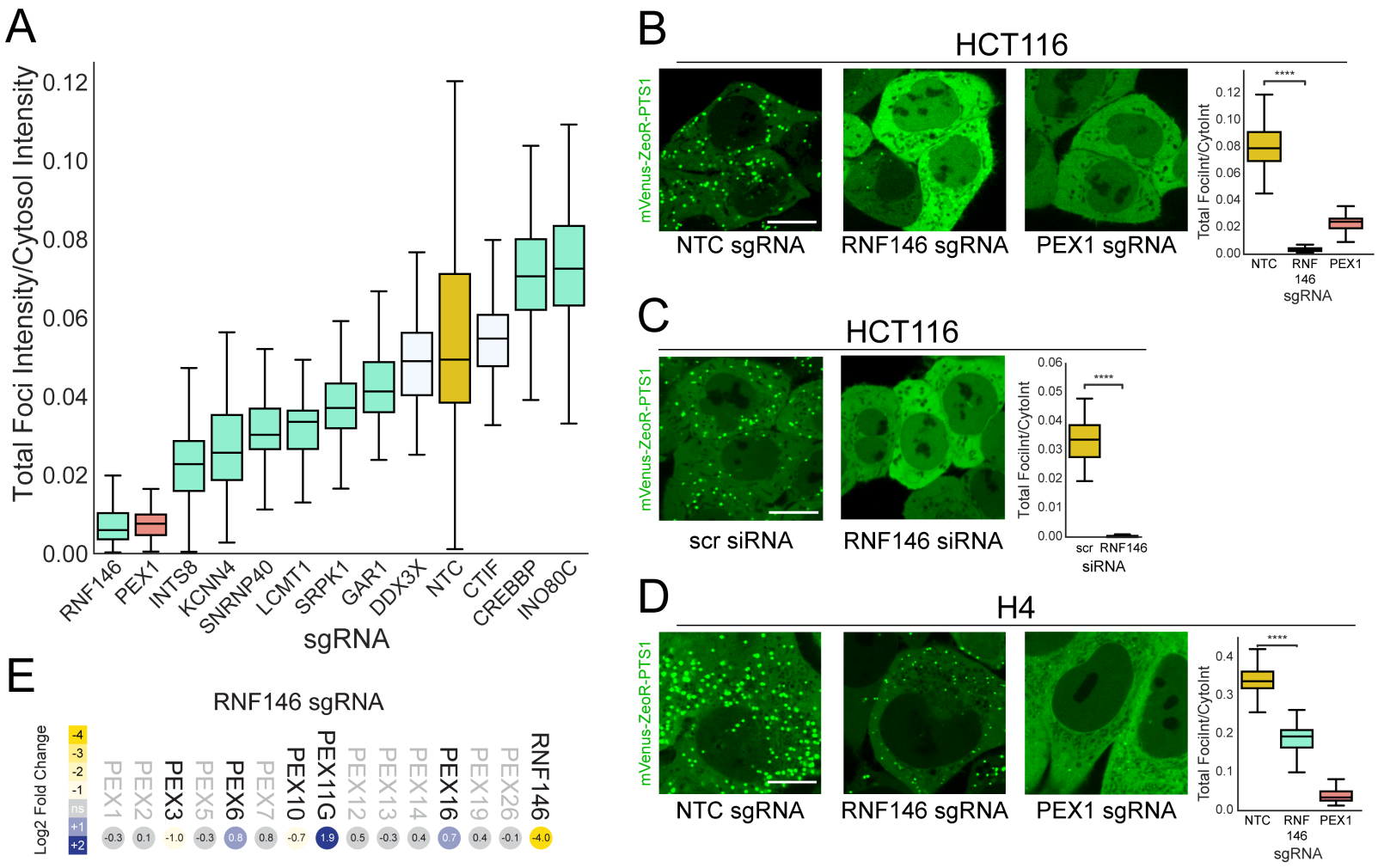
A
Total Foci Intensity/Cytosol Intensity
0.00
0.02
0.04
0.06
0.08
0.10
0.12
RNF146
PEX1
INTS8
KCNN4
SNRNP40
LCMT1
SRPK1
GAR1
DDX3X
NTC
CTIF
CREBBP
INO80C
sgRNA
B
HCT116
mVenus-ZeoR-PTS1
NTC sgRNA
RNF146 sgRNA
PEX1 sgRNA
Total FociInt/CytoInt
****
NTC
RNF 146 sgRNA
PEX1
C
HCT116
mVenus-ZeoR-PTS1
scr siRNA
RNF146 siRNA
Total FociInt/CytoInt
****
scr
RNF146 siRNA
D
H4
mVenus-ZeoR-PTS1
NTC sgRNA
RNF146 sgRNA
PEX1 sgRNA
Total FociInt/CytoInt
****
NTC
RNF 146 sgRNA
PEX1
E
RNF146 sgRNA
Log2 Fold Change
-4
-3
-2
-1
ns
+1
+2
PEX1 -0.3
PEX2 0.1
PEX3 -1.0
PEX5 -0.3
PEX6 0.8
PEX7 0.8
PEX10 -0.7
PEX11G 1.9
PEX12 0.5
PEX13 -0.3
PEX14 0.4
PEX16 0.7
PEX19 0.4
PEX26 -0.1
RNF146 -4.0

Figure 3

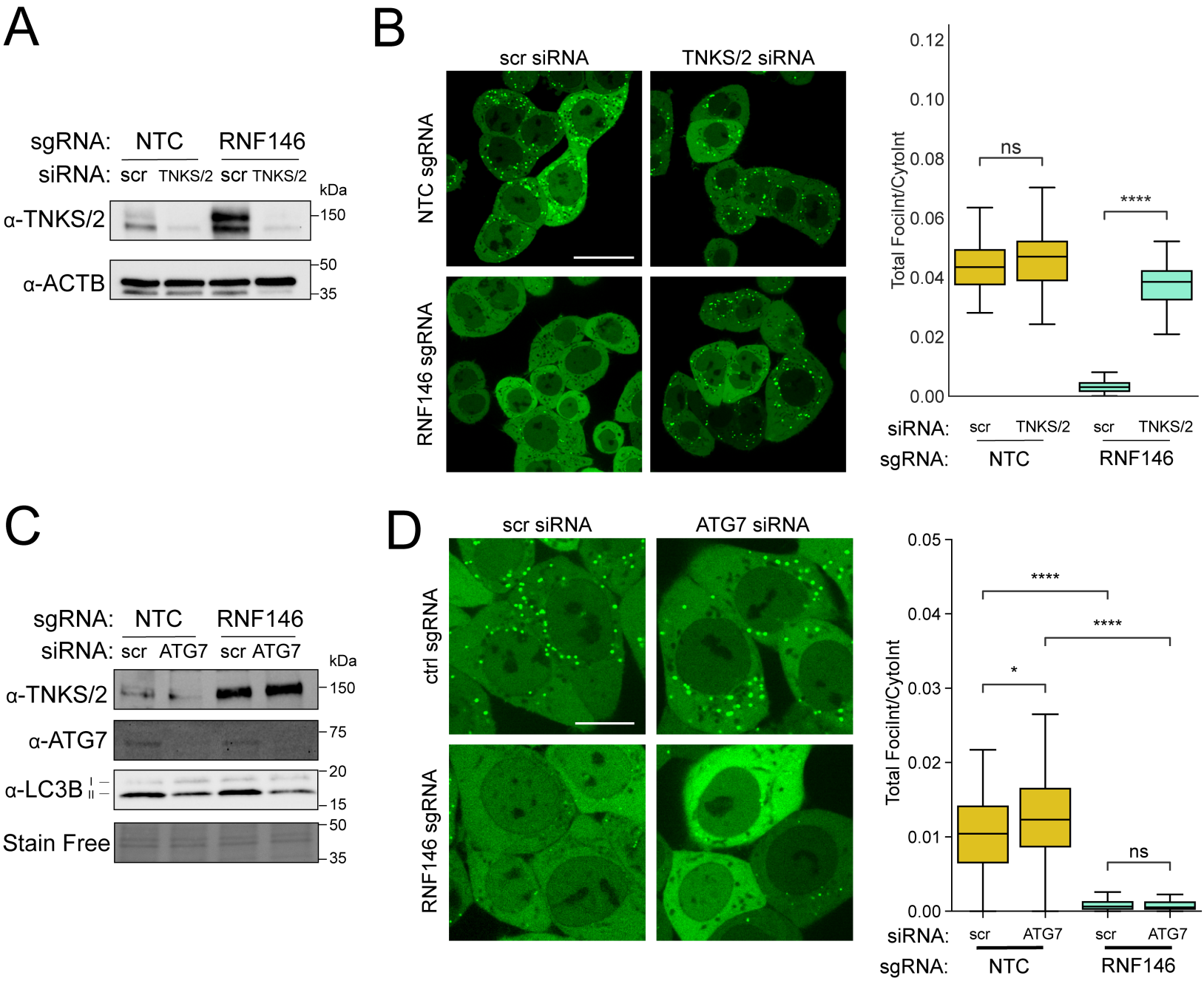
A
sgRNA: NTC RNF146
siRNA: scr TNKS/2 scr TNKS/2
kDa
α-TNKS/2
150
α-ACTB
50
35
B
scr siRNA
TNKS/2 siRNA
NTC sgRNA
RNF146 sgRNA
Total FociInt/CytoInt
0.12
0.10
0.08
0.06
0.04
0.02
0.00
ns
****
siRNA: scr TNKS/2 scr TNKS/2
sgRNA: NTC RNF146
C
sgRNA: NTC RNF146
siRNA: scr ATG7 scr ATG7
kDa
α-TNKS/2
150
α-ATG7
75
α-LC3B I II
20
15
Stain Free
50
35
D
scr siRNA
ATG7 siRNA
ctrl sgRNA
RNF146 sgRNA
Total FociInt/CytoInt
0.05
0.04
0.03
0.02
0.01
0.00
****
****
*
ns
siRNA: scr ATG7 scr ATG7
sgRNA: NTC RNF146

Figure 4

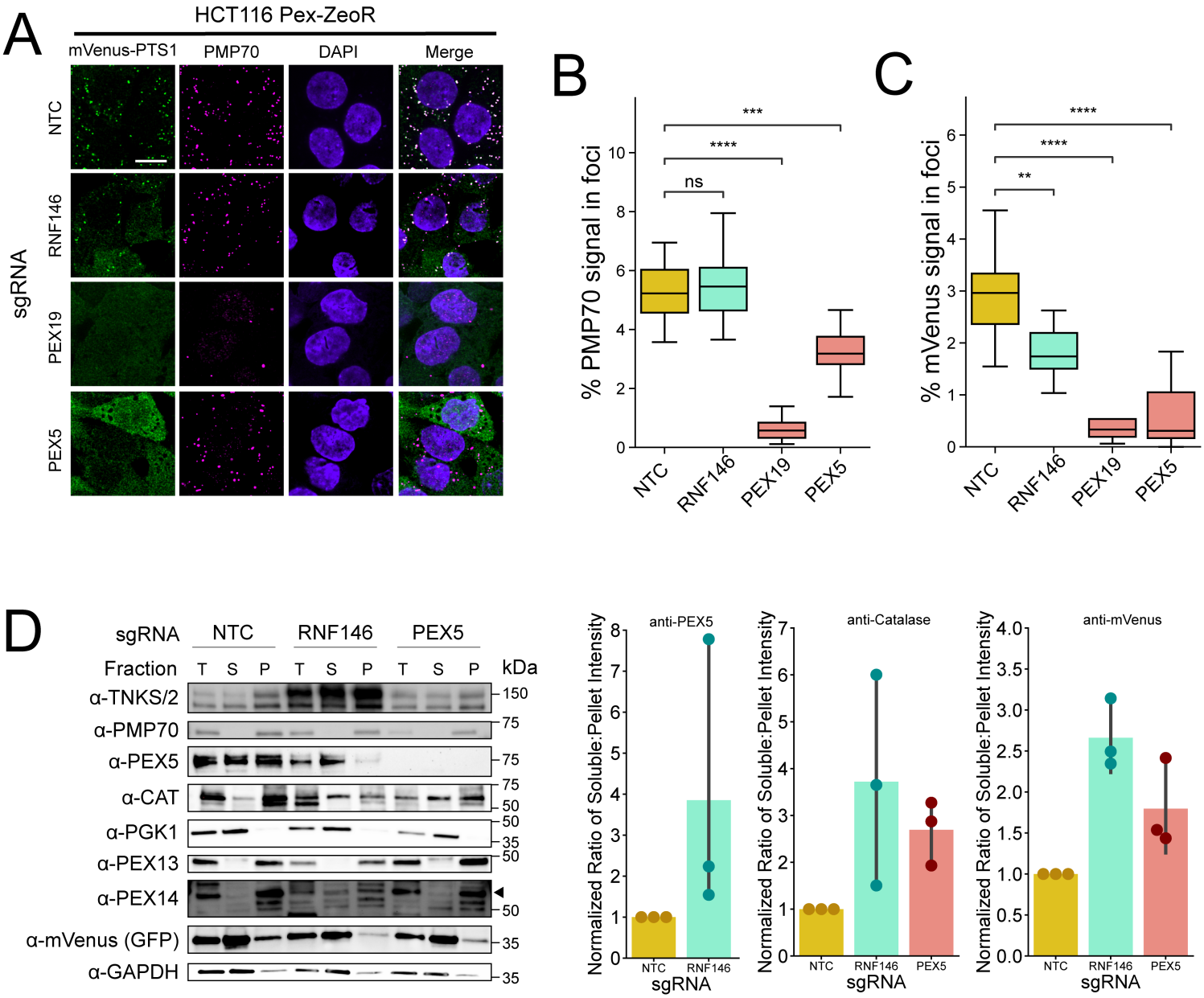
A
HCT116 Pex-ZeoR
mVenus-PTS1
PMP70
DAPI
Merge
sgRNA
NTC
RNF146
PEX19
PEX5
B
% PMP70 signal in foci
***
****
ns
NTC
RNF146
PEX19
PEX5
C
% mVenus signal in foci
****
****
**
NTC
RNF146
PEX19
PEX5
D
sgRNA
NTC
RNF146
PEX5
Fraction
T S P T S P T S P
kDa
α-TNKS/2
α-PMP70
α-PEX5
α-CAT
α-PGK1
α-PEX13
α-PEX14
α-mVenus (GFP)
α-GAPDH
150
75
75
75
50
50
35
50
50
35
35
anti-PEX5
anti-Catalase
anti-mVenus
Normalized Ratio of Soluble:Pellet Intensity
NTC
RNF146
PEX5
sgRNA

Figure 5

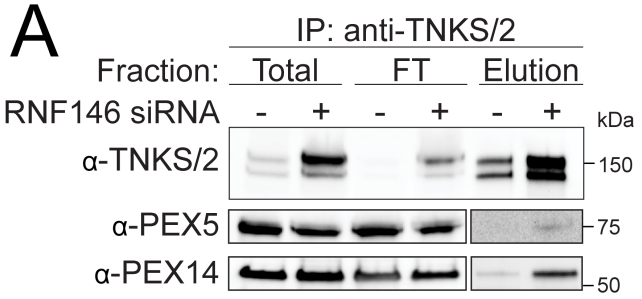
A
IP: anti-TNKS/2
Fraction:
Total
FT
Elution
RNF146 siRNA
- + - + - +
kDa
α-TNKS/2
α-PEX5
α-PEX14
150
75
50

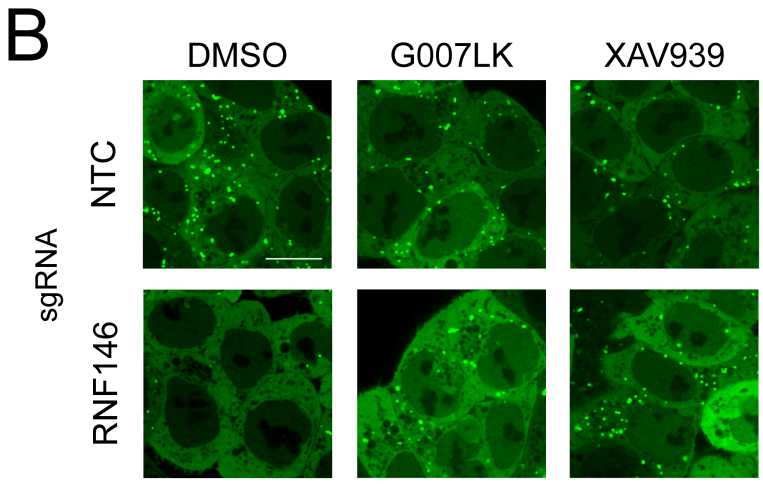
B
DMSO
G007LK
XAV939
sgRNA
NTC
RNF146

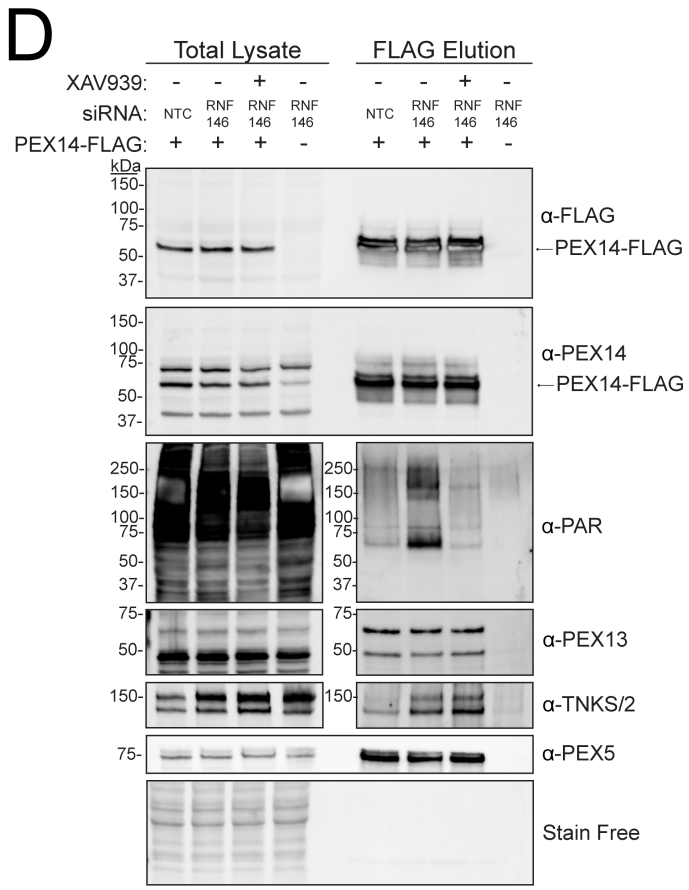
D
Total Lysate
FLAG Elution
XAV939:
siRNA:
NTC
RNF 146
PEX14-FLAG:
kDa
α-FLAG
←PEX14-FLAG
α-PEX14
←PEX14-FLAG
α-PAR
α-PEX13
α-TNKS/2
α-PEX5
Stain Free

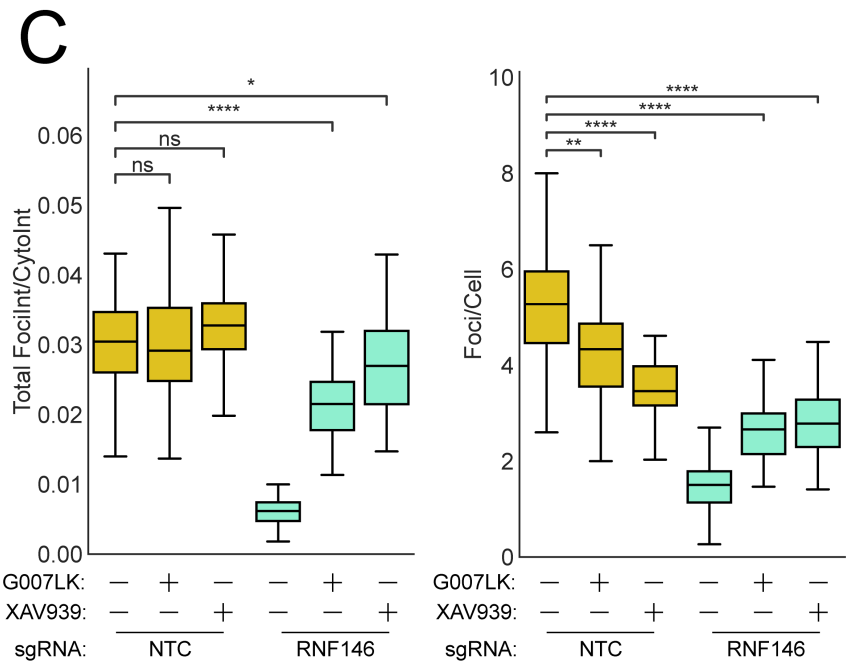
C
Total FociInt/CytoInt
Foci/Cell
ns
*
**
****
G007LK:
XAV939:
sgRNA:
NTC
RNF146

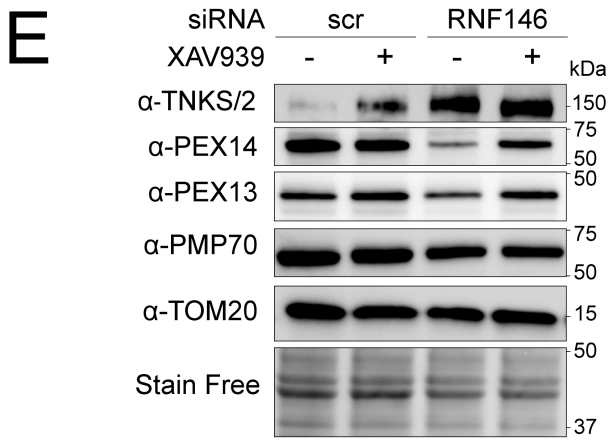
E
siRNA
scr
RNF146
XAV939
kDa
α-TNKS/2
α-PEX14
α-PEX13
α-PMP70
α-TOM20
Stain Free

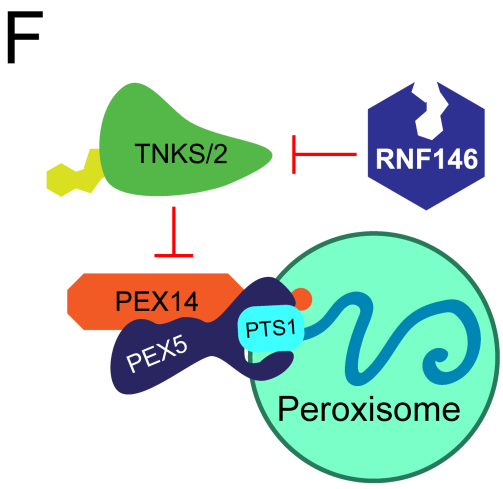
F
TNKS/2
RNF146
PEX14
PEX5
PTS1
Peroxisome

Figure 6

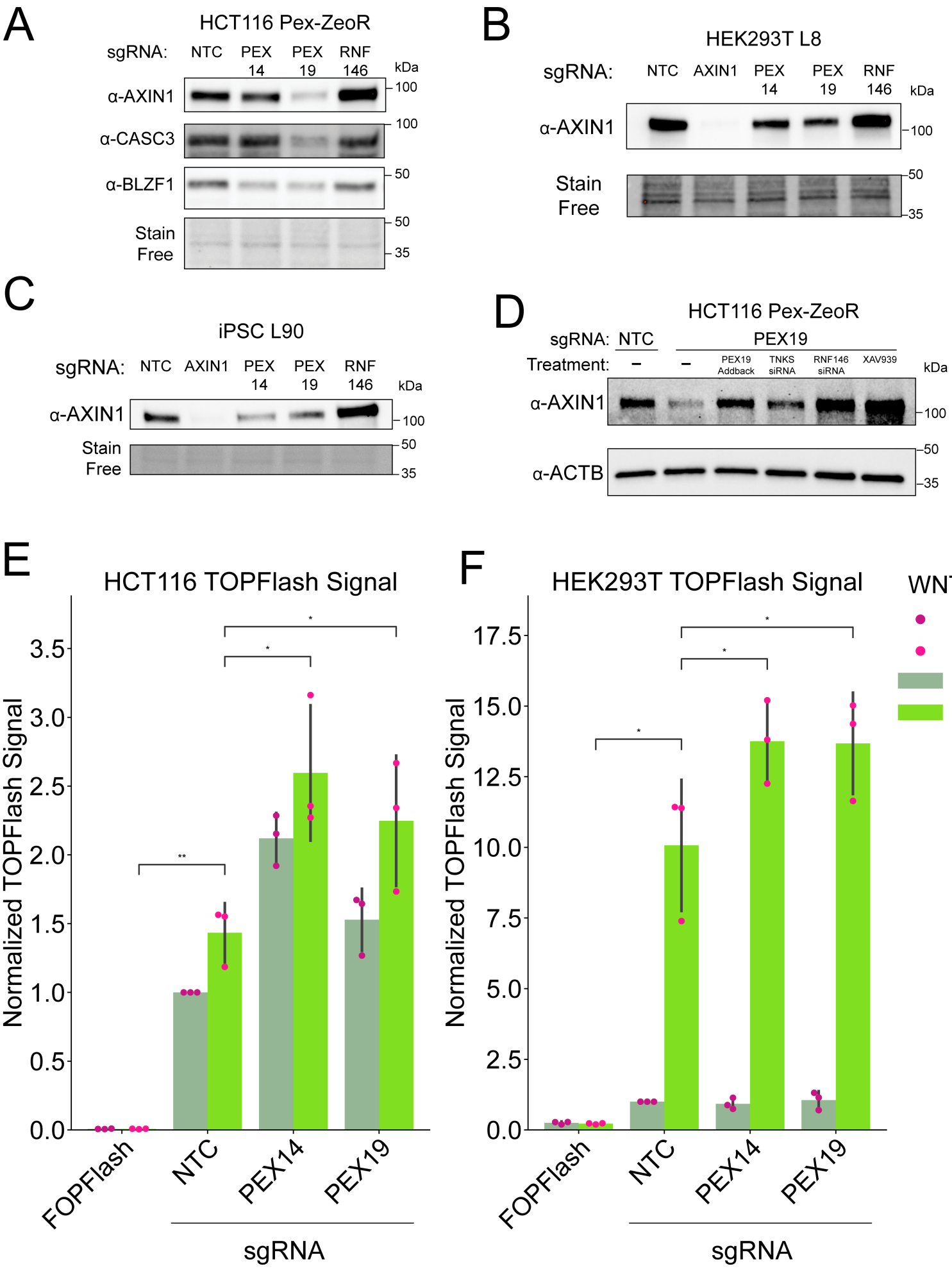
A
HCT116 Pex-ZeoR
sgRNA: NTC PEX 14 PEX 19 RNF 146
kDa
α-AXIN1
α-CASC3
α-BLZF1
Stain Free
100
100
50
50
35
B
HEK293T L8
sgRNA: NTC AXIN1 PEX 14 PEX 19 RNF 146
kDa
α-AXIN1
Stain Free
100
50
35
C
iPSC L90
sgRNA: NTC AXIN1 PEX 14 PEX 19 RNF 146
kDa
α-AXIN1
Stain Free
100
50
35
D
HCT116 Pex-ZeoR
sgRNA: NTC PEX19
Treatment: – – PEX19 Addback TNKS siRNA RNF146 siRNA XAV939
kDa
α-AXIN1
α-ACTB
100
50
35
E
HCT116 TOPFlash Signal
Normalized TOPFlash Signal
3.5
3.0
2.5
2.0
1.5
1.0
0.5
0.0
FOPFlash
NTC
PEX14
PEX19
sgRNA
F
HEK293T TOPFlash Signal
WNT
Normalized TOPFlash Signal
17.5
15.0
12.5
10.0
7.5
5.0
2.5
0.0
FOPFlash
NTC
PEX14
PEX19
sgRNA

Supplementary Figure 1

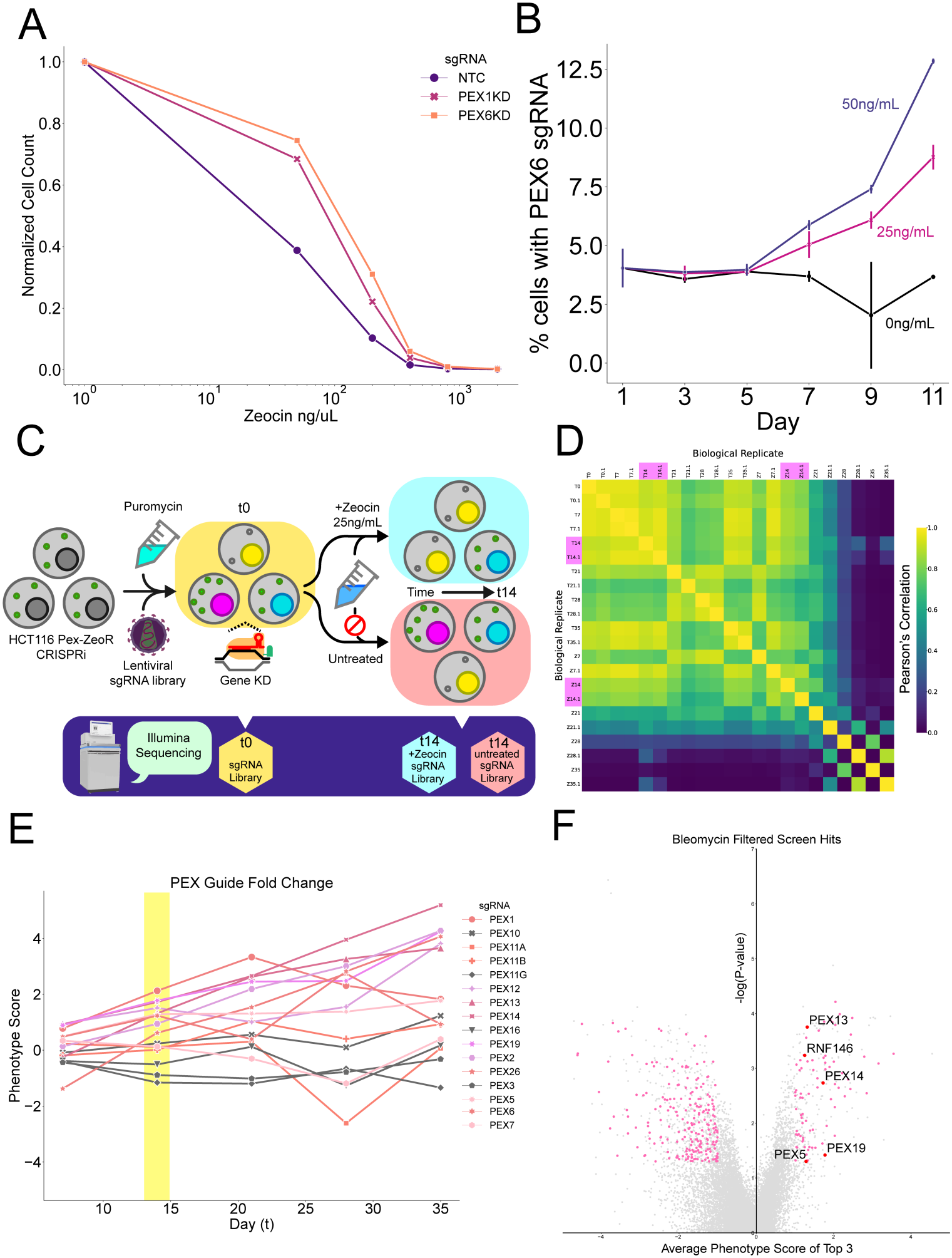

Supplementary Figure 2

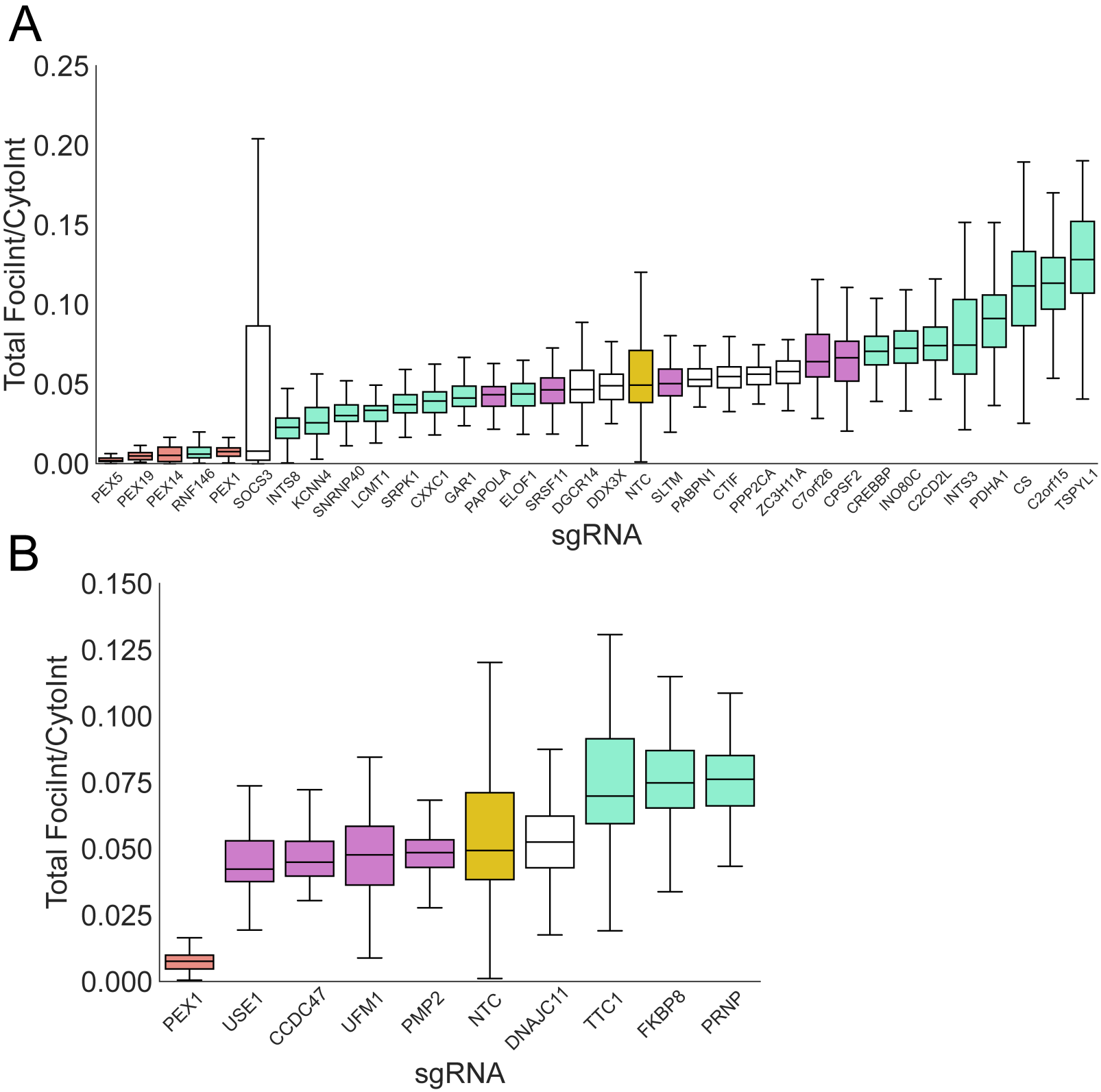

Supplementary Figure 3

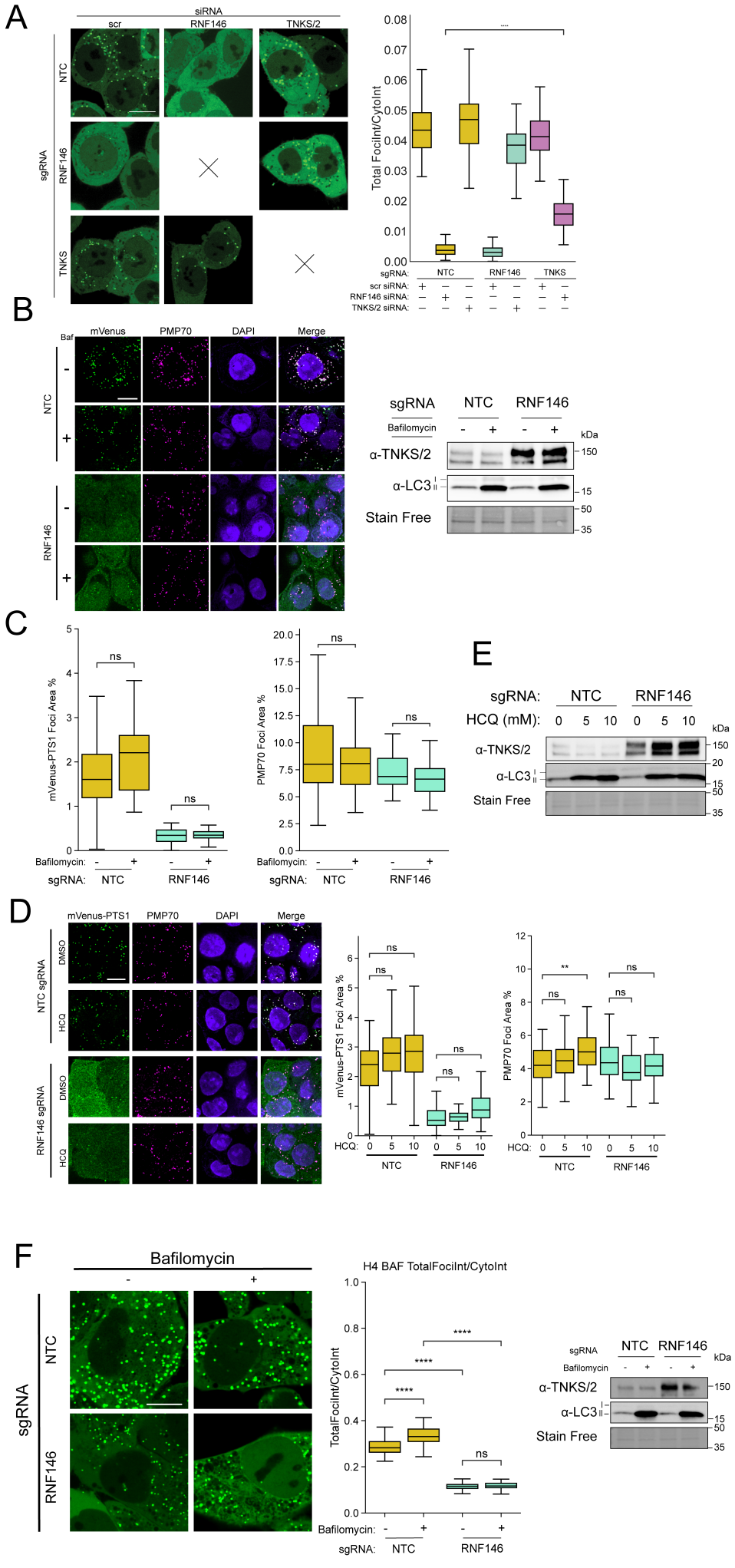

Supplementary Figure 4

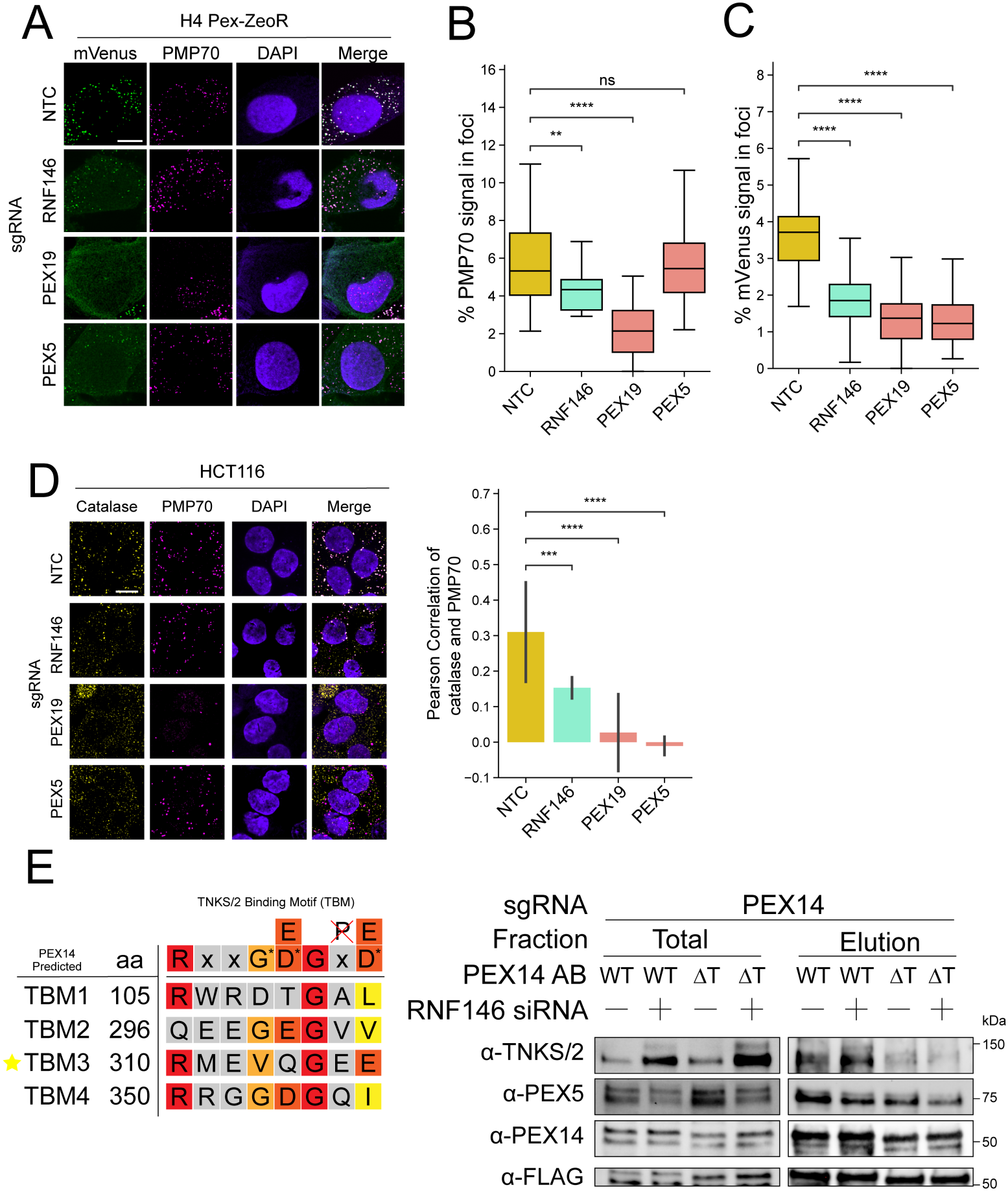

Supplementary Figure 5